

Deep learning-driven likelihood-free parameter inference for 21-cm forest observations

Tian-Yang Sun¹, Yue Shao¹, Yichao Li¹, Yidong Xu^{2,3} & Xin Zhang^{1,4,5,*}

¹*Key Laboratory of Cosmology and Astrophysics (Liaoning) & College of Sciences, Northeastern University, Shenyang 110819, China*

²*National Astronomical Observatories, Chinese Academy of Sciences, Beijing 100101, China*

³*Key Laboratory of Radio Astronomy and Technology, Chinese Academy of Sciences, Beijing 100101, China*

⁴*National Frontiers Science Center for Industrial Intelligence and Systems Optimization, Northeastern University, Shenyang 110819, China*

⁵*Key Laboratory of Data Analytics and Optimization for Smart Industry (Ministry of Education), Northeastern University, Shenyang 110819, China*

The hyperfine structure absorption lines of neutral hydrogen in spectra of high-redshift radio sources, known collectively as the 21-cm forest, have been demonstrated as a sensitive probe to the small-scale structures governed by the dark matter (DM) properties, as well as the thermal history of the intergalactic medium regulated by the first galaxies during the epoch of reionization. By statistically analyzing these spectral features, the one-dimensional (1D) power spectrum of the 21-cm forest can effectively break the parameter degeneracies and constrain the properties of both DM and the first galaxies. However, conventional parameter inference methods face challenges due to computationally expensive simulations for

21-cm forest and the non-Gaussian signal characteristics. To address these issues, we introduce generative normalizing flows for data augmentation and inference normalizing flows for parameters estimation. This approach efficiently estimates parameters from minimally simulated datasets with non-Gaussian signals. Using simulated data from the upcoming Square Kilometre Array (SKA), we demonstrate the ability of the deep learning-driven likelihood-free approach to generate accurate posterior distributions, providing a robust and efficient tool for probing DM and the cosmic heating history using the 1D power spectrum of 21-cm forest in the era of SKA. This methodology is adaptable for scientific analyses with other unevenly distributed data.

The hyperfine structure transition of neutral hydrogen atoms from the epoch of reionization (EoR) creates narrow absorption lines on spectra of high-redshift radio bright sources (e.g. radio-loud quasars), with a rest-frame wavelength of 21 cm. The 21-cm absorption lines from various structures at different distances along the line of sight are redshifted to different frequencies, giving rise to forest-like features on the spectra, which is called the 21-cm forest¹⁻⁶ in analogy to the Lyman- α (Ly- α) forest at lower redshifts. The 21-cm forest has been demonstrated to be a sensitive probe of the cosmic heating history^{4,5}. After the formation of the first galaxies, the generated light not only ionizes hydrogen atoms but also heats the gas simultaneously (with X-rays being the primary heating source). As the spin temperature of the gas increases, the absorption at 21 cm weakens (reducing the optical depth), thus causing the 21-cm forest signal to become weaker. In principle, the strength of the signal can be used to measure the cosmic heating history, thereby gaining insight into the properties of the first galaxies.

On the other hand, understanding the properties of dark matter (DM) hinges crucially on probing small-scale structures of the universe. The cold DM leads to an excess of structure on small scales, while warm DM (WDM) or ultra-light DM results in suppressed structure formation on small scales^{7,8}. Being sensitive to the small-scale structures, it has been shown that the 21-cm forest can be used to probe the minihalos and dwarf galaxies during the EoR^{5,9}, so as to provide precise measurements of small-scale cosmic structures, and can be utilized to measure the mass of DM particles¹⁰.

During the Square Kilometre Array (SKA) era, conducting 21-cm forest observations theo-

retically allows the mass of DM particles to be constrained based on the number density of absorption lines^{2,10}. However, detecting the 21-cm signal is by no means an easy task. In particular, if the extent of cosmic heating is too strong, it will render the 21-cm forest signal undetectable, thereby making it impossible to measure either the properties of DM particles or the temperature of the intergalactic medium (IGM) through this method.

Our recent work has proposed an effective solution to this problem, namely, by measuring the one-dimensional (1D) power spectrum of the 21-cm forest¹¹. This approach not only allows for the extraction of faint signals but also breaks the degeneracy between the mass of DM particles and the temperature of the IGM, enabling both to be measured simultaneously. This is because, when transforming from frequency space to k -space, the scale-dependence characteristics of the 21-cm forest signal can be displayed, while noise can be effectively suppressed as it lacks such scale dependence, enabling even faint signals to be extracted. Furthermore, the properties of DM particles (whether warm or cold) and the temperature of the IGM mainly affect the shape and amplitude of the power spectrum, respectively. Thus, both can be simultaneously constrained through power spectrum measurements. If this approach can be successfully implemented during the SKA era, it will be significant for research of DM and first galaxies.

To achieve this goal, a series of challenges still need to be overcome. Observationally, it requires a sufficiently sensitive experiment and long observation times to detect the weak signals, as well as a sufficient number of high-redshift radio-bright point sources to suppress the cosmic variance. Additionally, even if we can achieve 21-cm forest observations, it is not straightforward

to constrain the properties of DM particles and the cosmic heating history, because currently there is no analytical or empirical model to connect the parameters (such as the mass of DM particles and the temperature of the IGM) with observables (the 1D power spectrum of the 21-cm forest). In this case, in order to achieve parameter inference, we can only rely on a large number of simulations spanning a sufficient large parameter space to calculate observables, and then further construct a likelihood function, thus utilizing Bayesian methods for parameter inference¹². This is how parameter inference is done for constraining DM particles using the Ly- α forest¹³. Such a large number of simulations require a significant amount of computing resources, making it both very expensive and extremely time-consuming. Moreover, the computational costs for the 21-cm forest simulations are considerably higher due to its major contributions from smaller scales (k as high as $\sim 100 \text{ Mpc}^{-1}$), compared to the Ly- α forest^{2,14}.

Additional challenges arise from the non-Gaussianity of the 21-cm forest signals induced by the nonlinear effect of gravitational clustering¹⁵ and the non-local effect of radiation¹⁶. Due to the non-Gaussian characteristics of the 1D power spectrum, traditional Bayesian methods for parameter inference are somewhat inadequate, potentially leading to severely distorted inference results. Although methods like traditional Gaussian mixture models can fit likelihood functions under non-Gaussian conditions^{17,18}, they require significant computational resources, making them less practical for extensive data analysis. Additionally, the correlation between the 1D power spectrum at different scales also affects the precision of parameter inference by coupling errors across scales.

This work proposes a set of solutions to these issues, allowing parameter inference of 21-cm forest observations without the need for an explicit model or the construction of the likelihood function, using only a limited number of simulated samples. This enables us to obtain constraints on the properties of DM particles and the history of cosmic heating efficiently from 1D power spectrum measurements of the 21-cm forest. The key strategy relies on variational inference methods based on deep learning¹⁹, especially the technique of normalizing flows (NFs)²⁰. These methods have found various applications in fields such as the large-scale generation of neutral hydrogen sky maps^{21,22}, parameters inference during the EoR using 21-cm tomography^{23–26}, inference of gravitational wave source parameters under the influence of noise transients^{27,28}, and the inference of the IGM thermal parameters based on the Ly- α forest^{29,30}. Within this framework, not only can a large number of simulated samples be easily generated through generative neural networks, but parameter inference can also be achieved without a likelihood function. This approach addresses the aforementioned challenges of large sample sizes and non-Gaussianity, respectively, for 21-cm forest observations, paving the way for advancing the usage of this probe to constrain the fundamental physics during the cosmic dawn.

Results

We take the same approach as in Ref.¹¹, and simulate the 21-cm forest signals from the EoR for various X-ray production efficiency of the first galaxies parameterized by f_X , and for various DM particle masses of m_{WDM} (see Methods). Given the current Hydrogen Epoch of Reionization Array findings, T_K is constrained to $15.6 \text{ K} < T_K < 656.7 \text{ K}$ at $z \sim 8$ with 95% confidence³¹,

which demarcates the rough signal level of the 21-cm forest constrained by the heating effect. Therefore, our analysis mainly focus on two characteristic heating levels for discussion: the case with a weaker heating effect ($T_K \approx 60$ K at redshift 9 corresponding to $f_X \sim 0.1$) and the case with a stronger heating effect ($T_K \approx 600$ K at redshift 9 corresponding to $f_X \sim 1$). For comparison, we also simulate cases with $f_X = 0$ representing an unheated IGM and $f_X = 3$ for an extremely high productivity of X-rays in the early universe. For the DM properties, recent astrophysical observations have put a lower limit on WDM particle mass (m_{WDM}) to a few kilo electronvolts (keV)^{32–36}, and almost ruled out models below 3 keV³⁶. Therefore, m_{WDM} ranges from 3 keV to 9 keV in our simulation. Assuming a fiducial WDM model with $m_{\text{WDM}} = 6$ keV, Fig. 1 shows the signal-to-noise ratio (SNR) of the 1D power spectrum of the simulated 21-cm forest, represented by $P(k)/P^N$, with different heating levels for phase-one and phase-two low-frequency array of the SKA (SKA1-LOW and SKA2-LOW), respectively. Our results indicate that a lower heating level ($T_K = 60$ K at $z = 9$) allows for measurement of the 1D power spectrum of the 21-cm forest with an integration time of 100 h per background source using the SKA1-LOW. In contrast, a higher heating level ($T_K = 600$ K at $z = 9$) necessitates 200 h on each source using SKA2-LOW.

Given the high dynamic range required for the 21-cm forest simulations, the simulation-based Bayesian methods for parameter inference are inefficient and almost infeasible, considering the requirement of computational time and resources. To achieve parameter inference with minimal computational expenditure, we first simulate the 21-cm forest signals for a limited sampling of the parameter space. However, the unevenness in simulated data will impair likelihood-free inference methods, potentially leading to inaccurate probability estimations within certain parameter

spaces presented in Supplementary Fig. 1. To address this, we employ data augmentation using the generative normalizing flow (GNF) to expand the coverage of our datasets beyond the simulated parameter space, thus improving the accuracy of parameter inference results of the subsequent inference normalized flow (INF). The flow chart of our methodology is presented in Fig. 2.

To guarantee a robust parameter inference, we first assess the reliability of the 1D power spectrum of the 21-cm forest generated by the GNF. Figure 3 compares the mean value and standard deviation of the 1D power spectra generated by the GNF with those from simulations. The results confirm that the GNF consistently reproduces the 1D power spectra generated from the training set as presented in the middle panels of Fig. 3. In addition, it effectively generates the 1D power spectra for both interpolated and extrapolated parameter regions as presented in the left and right panels of Fig. 3, demonstrating its generalization capability. To quantify the reasonableness of the GNF model, we applied the coefficient of determination (R^2) to measure the correlation between the 1D power spectra generated by the GNF and those from simulations. Achieving $R^2 > 0.99$ indicates a high reliability of the GNF in reproducing these 1D power spectra. This examination, combining statistical measures and visual inspections, confirms the reliability of the GNF model in generating the 1D power spectrum of the 21-cm forest.

We used the skewness coefficient (S) to describe the asymmetry of the 1D power spectrum at each k in Fig. 4. It shows that at smaller scales and with longer integration times, deviations from a Gaussian distribution increase. This trend is attributed to strong nonlinear effects and a higher proportion of sample variance compared to the observational uncertainty. Additionally, we observed

gradual deviations from a normal distribution with increasing m_{WDM} and T_{K} . These deviations are attributed to the increased number of halos with higher m_{WDM} , which significantly alters the density field, and to temperature variations influencing the 1D power spectrum of the 21-cm forest as T_{K} increases. Additionally, we quantified the similarity between the distributions generated by the GNF and the simulation in Supplementary Fig. 2 using the Jensen-Shannon divergence (JSD)^{37,38}, a symmetric measure of similarity between two probability distributions. Our analysis revealed that the JSD value is less than 0.05, indicating a high degree of similarity between the distributions generated by the GNF and the simulation. As previously noted with JSD and S analyses, these findings further confirm that under different heating levels, the 1D power spectrum of the 21-cm forest observed with an integration time of 100 h using SKA1-LOW and those measured with an integration time of 200 h using SKA2-LOW exhibit Gaussian and non-Gaussian distributions, respectively. This highlights the capability of the GNF in modeling the 1D power spectrum of the 21-cm forest under various astrophysical conditions.

The correlation coefficient ρ_{ij} between different k bins of the 1D power spectrum of the 21-cm forest is also crucial for accurately estimating the uncertainties in parameter inference. Here, i and j refer to different k bins. Ignoring the correlation in the 1D power spectrum between these different k bins can lead to incorrect error estimates. In supplementary Fig. 3, we show the values of ρ_{ij} of the pure signal under different conditions. We find that the correlations at small scales are significant, especially in scenarios with strong heating effects. However, considering the impact of SKA thermal noise in actual observations, as shown in supplementary Fig. 4, the dominance of thermal noise at small scales reduces the overall correlation strength. Nonetheless, the correlations

remain non-negligible.

First, we need to determine the accuracy of the INF inference parameters. Given the lack of tight constraints on m_{WDM} and T_{K} , we explored arbitrary parameter results using the INF in Fig. 5. Our results show that the recovery is mostly near perfect. Next, we determine the precision of the parameters inferred by INF. Similar to findings in Refs.^{24,29}, we encounter challenges due to the edge effect, which makes inferences at the boundaries of the parameter space unreliable. However, this can be achieved by expanding the coverage of the simulated parameter space. However, within the central regions of the parameter space, our analysis reveals distinct patterns in the relative error ε of parameter inference for m_{WDM} and T_{K} under various heating levels, as presented in Supplementary Fig. 5. Here, the relative error, defined as the precision, is given by $\varepsilon(\xi) = \sigma(\xi)/\xi$, where ξ represents the true parameter (m_{WDM} or T_{K}). We find that T_{K} significantly affects the precision of m_{WDM} estimates. Conversely, m_{WDM} has a relatively small impact on the precision of T_{K} estimates. This is because T_{K} influences the 1D power spectrum values across all scales, while m_{WDM} primarily affects the 1D power spectrum values on small scales, as shown in Supplementary Fig. 6. Therefore, as presented in Supplementary Fig. 7, T_{K} can achieve high precision by relying solely on large-scale information, almost unaffected by m_{WDM} . On the other hand, m_{WDM} mainly relies on small-scale and medium-scale information, which is influenced by T_{K} . Therefore, the 1D power spectrum of different scales will break the degeneracy, resulting in a significant improvement in the precision of parameter estimates. This dependence highlights the interplay between these parameters and emphasizes the ability of our network to effectively constrain each parameter.

For low heating level conditions, we utilized SKA1-LOW with an integration time of 100 h to examine the constraint results of posterior parameter inference, assuming $m_{\text{WDM}} = 6$ keV and $T_{\text{K}} = 60$ K. We compared the precision of the posterior inference results from the INF with the range predicted by the Fisher matrix as presented in Fig. 6. The INF method successfully recovered the posterior distribution of parameters, with the true values lying within the estimated 1σ confidence region. This demonstrates precision comparable to the predictions of the Fisher matrix. The final average constraint result of the 1D power spectra of the 21-cm forest for all simulations are $m_{\text{WDM}} = 6.28^{+1.61}_{-1.59}$ keV and $T_{\text{K}} = 60.17^{+6.16}_{-6.66}$ K. Detailed simulations of the dataset are described in the Methods section. This confirms the reliability of the INF method in achieving precise parameter inference under low heating conditions.

Under high heating level conditions, using SKA2-LOW with an integration time of 200 h ($m_{\text{WDM}} = 6$ keV, $T_{\text{K}} = 600$ K), we observed significantly different results. Although both the Fisher matrix and INF methods presented consistent degeneracy directions, the Fisher matrix approach failed to adequately constrain the parameters due to the non-Gaussian characteristic of the 1D power spectrum of the 21-cm forest. This highlights the effectiveness of likelihood-free inference methods like the INF in such scenarios. The final average constraint results of the 1D power spectra for all simulations are $m_{\text{WDM}} = 6.47^{+2.04}_{-1.88}$ keV and $T_{\text{K}} = 627.95^{+94.18}_{-91.07}$ K. These results demonstrate that, while the Fisher matrix approach is inadequate under non-Gaussian conditions, the INF method remains effective.

To confirm the reliability of our parameter estimates, we conducted the Kolmogorov-Smirnov

(KS) test³⁹. The KS test is a non-parametric test that compares the cumulative distribution function (CDF) of the sample data to a reference distribution. By computing the CDF of the percentiles of the true values of each parameter derived from the marginal 1D posterior distribution, we can evaluate the model’s performance. For each 21-cm forest 1D power spectrum and the corresponding confidence interval of the posterior distribution, the percentile values of the injected parameters are computed. Ideally, the CDF for each parameter should be close to the diagonal, as the percentiles should be evenly distributed between 0 and 1. We measured the CDF of the true parameters falling within specific confidence levels as presented in Supplementary Fig. 8. The results demonstrated the CDF curves within the 3σ confidence bands, with p -values greater than 0.05 for each parameter. A KS test p -value greater than 0.05 indicates that there is no significant difference between the CDF of the sample data and the reference distribution, confirming that the observed deviations are within the expected range due to random sampling variability. These findings affirm the validity and accuracy of our inference method within the expected error ranges, providing confidence in its application for cosmological studies. The KS test results support the reliability of our approach in accurately estimating m_{WDM} and T_{K} , ensuring that our method is theoretically sound and practically reliable.

Discussion

Observing the 21-cm forest signals during the EoR provides a valuable opportunity to gain insight into DM properties and the heating history in the first billion years of the universe. However, due to the lack of explicit relation between the physical parameters and the observables,

parameter inference has been impeded by the limited parameter space covered by computationally expensive simulations and the infeasible requirement on computational resources. Moreover, the non-Gaussian characteristic of the 21-cm forest signal complicates the evaluation of the likelihood function, resulting in biased inference of parameters. In this paper, we introduce a deep learning-based approach that enables model-independent inference of T_K and m_{WDM} with a small number of simulations. Notably, this approach could extend to non-Gaussian scenarios, allowing for parameter inference using arbitrary 21-cm forest signals.

Furthermore, the deep learning-based parameter inference method presented in this work demonstrates innovation and effectiveness not only in astronomy and cosmology but also in handling complex and unbalanced datasets⁴⁰. For example, in biomedical research, where sample scarcity hampers understanding of rare diseases⁴¹, our advanced data analysis technology can significantly enhance data analysis capabilities and drive scientific discovery. With ongoing algorithm optimization and advancements in computing power, this method is poised to play a pivotal role in advancing interdisciplinary research.

In our work, we employ the multi-scale modeling approach from Ref.¹¹ to simulate the 21-cm forest signal. We use `21cmFAST`⁴² to model the ionization field^{43,44} and density field^{45–48} on large scales, identifying neutral regions to simulate the 21-cm signal, with the density fields serving as initial conditions for small-scale simulations^{10,49–52}. The main contributors to the 21-cm signal are minihalos, modeled using the conditional halo mass function^{45,46} to estimate the number and distribution of low-mass minihalos, with a minimum halo mass of $10^6 M_\odot$, corresponding to

the filter mass⁵³ at the redshift of interest. Halo density profiles are calculated using the Navarro-Frenk-White (NFW) profile⁵⁴ within the virial radius and the infall model profile⁵⁵ outside it. The infall model, suitable for high-density areas with numerous halos, tends to overestimate the density field, requiring normalization of the field to match the initial local density of 21cmFAST outputs. The normalization technique of Ref.¹¹, which involves multiplying each voxel by a factor, alters the amplitude of the 1D power spectrum of the 21-cm forest and leads to a crossover in the 1D power spectrum across different DM models (See Fig. 3 in Ref.¹¹). To address this, we employ a normalization method that does not affect the amplitude of the 1D power spectrum, adjusting the density field by adding or subtracting a number. Furthermore, to maintain the probability density distribution of the density field, we adjust the lower limit of halo mass to $10^5 M_\odot$ in the simulation, corresponding to the Jeans mass⁵⁶ at the redshift of interest, which also mitigates anomalies in the 1D power spectrum on large scales. Figure 6 in Ref.¹¹ shows that the degeneracy direction between m_{WDM} and T_{K} is negatively correlated. As we previously discussed in Supplementary Fig. 7, different scales affect the degeneracy direction of the two parameters differently. In this work, the improvements we made have altered the relationship of the 1D power spectrum on large scales for different DM models. Consequently, in Fig. 6, the degeneracy direction between m_{WDM} and T_{K} becomes positively correlated. Meanwhile, using SKA2-LOW with an integration time of 100 h is insufficient to observe the 21-cm forest signal. As a result, we increased the integration time to 200 h.

For data analysis, we calculate the two-point correlation function of the 21-cm forest and convert it to the k -space, resulting in the 1D power spectrum along the line of sight. The choice

stems from the faintness of the 21-cm forest signal, making a power spectrum analysis more beneficial. Nonetheless, other studies²⁶ suggest alternative methods that could more effectively compress data and yield more precise parameter constraints. Future research will explore these methods for nearly lossless parameter inference, enhancing the effectiveness of constraints. Additionally, we plan to incorporate factors like metal absorption lines⁵⁷ coupling and foreground to create a more accurate dataset.

Overall, our study demonstrates that deep learning-based methods, particularly NFs, offer a promising approach to analyzing the 21-cm forest signal. These methods address the challenges of simulation data scarcity and complexity, providing robust and accurate parameter inference. As the SKA era approaches, these innovative techniques will be invaluable for extracting maximum scientific information from 21-cm observations, contributing to a deeper understanding of the thermal history of the universe and the properties of DM.

Methods

Simulations of the 1D power spectrum of the 21-cm forest. The differential brightness of the observed 21-cm absorption signal relative to the brightness temperature of the background radiation at a specific direction \hat{s} and redshift z is

$$\delta T_b(\hat{s}, \nu) \approx \frac{T_S(\hat{s}, z) - T_\gamma(\hat{s}, \nu_0, z)}{1 + z} \tau_{\nu_0}(\hat{s}, z), \quad (1)$$

where $\nu_0 = 1420.4$ MHz is the rest frame frequency of 21-cm photons, T_S is the spin temperature of HI gas, τ_{ν_0} is the 21-cm optical depth. In terms of average gas properties within each voxel, the 21-cm optical depth can be written as^{3,58,59}

$$\tau_{\nu_0}(\hat{s}, z) \approx 0.0085[1 + \delta(\hat{s}, z)](1 + z)^{3/2} \left[\frac{x_{\text{HI}}(\hat{s}, z)}{T_S(\hat{s}, z)} \right] \left[\frac{H(z)/(1 + z)}{dv_{\parallel}/dr_{\parallel}} \right] \left(\frac{\Omega_b h^2}{0.022} \right) \left(\frac{0.14}{\Omega_m h^2} \right), \quad (2)$$

where $\delta(\hat{s}, z)$, $x_{\text{HI}}(\hat{s}, z)$ and $H(z)$ are the gas overdensity, the neutral fraction of hydrogen and the Hubble parameter, respectively. $dv_{\parallel}/dr_{\parallel}$ is the inherent velocity projected along the line of sight gradient and we ignore this term in the simulation.

For the spin temperature, we assume that it is coupled to T_K ($T_S \approx T_K$). The gas temperature in each voxel is set by the thermal history of the early universe and its proximity to halos. In this study, our focus is on neutral regions, where X-ray penetration primarily heats the gas, and subsequently affects the 21-cm signals. When we consider an unheated IGM ($f_X = 0$), the temperature of gas outside the virial radius is mainly determined by the cosmic expansion. For the brightness temperature of the background radiation T_γ , our assumption is the same as Ref.¹¹, which is related to the flux density of the background source S_{150} . In this work, we consider 10 background sources

with $S_{150} = 10$ mJy at $z = 9$ and perform a total of 100 measurements on 10 comoving Mpc length segments along the line of sight in a neutral patch.

Using a hybrid multi-scale approach, we simulate the 21-cm forest during the EoR. We employ the 21 cmFAST to model large-scale structures in a $(1 \text{ Gpc})^3$ box with 500^3 grids, initialized by DM properties. Further, each grid with a length of 2 Mpc is subdivided into 500^3 voxels. These voxels are populated with halos based on initial densities and the conditional halo mass function influenced by the m_{WDM} . Density within each voxel follows either the NFW model or the infall model⁵⁵, depending on proximity to the nearest halo. The model is as presented in Ref.¹¹. Throughout the study, we adopted a set of cosmological parameters consistent with Planck 2018 results⁶⁰: $\Omega_{\text{m}} = 0.3153$, $\Omega_{\text{b}}h^2 = 0.02236$, $\Omega_{\Lambda} = 0.6847$, $h = 0.6736$ and $\sigma_8 = 0.8111$. Ω_{Λ} and σ_8 are the dark energy density parameter and the matter fluctuation amplitude, respectively.

Observational uncertainties in the 21-cm forest include thermal noise, sample variance, contaminating spectral structure of foreground sources in the chromatic side lobes, and bandpass calibration errors¹¹. Regarding the error consideration, we only consider the thermal noise of the interferometer array and the sample variance in the 1D power spectrum measurement as Ref.¹¹. The sample variance is generated by the simulation process and does not need to be added separately. When measuring individual absorption lines directly, the noise flux density averaged over the two polarizations can be expressed as⁶¹

$$\delta S^{\text{N}} \approx \frac{2k_{\text{B}}T_{\text{sys}}}{A_{\text{eff}}\sqrt{2\delta\nu\delta t}}, \quad (3)$$

where A_{eff} is the effective collection area of the telescope, T_{sys} is the system temperature, $\delta\nu$ is the

channel width, δt is the integration time. The corresponding thermal noise temperature is

$$\delta T^{\text{N}} = \delta S^{\text{N}} \left(\frac{\lambda_z^2}{2k_{\text{B}}\Omega} \right) \approx \frac{\lambda_z^2 T_{\text{sys}}}{A_{\text{eff}}\Omega\sqrt{2\delta\nu\delta t}}, \quad (4)$$

where λ_z is the observation wavelength, $\Omega = \pi(\theta/2)^2$ is the solid angle of the telescope beam, where $\theta = 1.22\lambda_z/D$ is the angular resolution, D is the longest baseline of a radio telescope or array. For SKA1-LOW, we use $A_{\text{eff}}/T_{\text{sys}} = 800 \text{ m}^2/\text{K}^{62}$. For SKA2-LOW, we use $A_{\text{eff}}/T_{\text{sys}} = 4,000 \text{ m}^2/\text{K}^{63}$. For these two arrays, we assume $D = 65 \text{ km}$, and the integration time δt is 100 h and 200 h, respectively.

In Supplementary Fig. 9, we calculated the brightness temperature for different cases. Direct measurement of individual absorption lines is easily hampered by early X-ray heating. To improve the sensitivity of detecting the 21-cm forest signal and reveal the clustering properties of the absorption lines to distinguish the effect on the 21-cm signal between the heating effect and WDM model, we followed the algorithm in Ref.¹¹ and calculated 1D power spectrum of brightness temperature under the assumption of high redshift background sources⁶⁴. The brightness temperature $\delta T_{\text{b}}(\hat{\mathbf{s}}, \nu)$ as a function of the observation frequency ν can be equivalently used as the line-of-sight distance r_z , $T'_{\text{b}}(\hat{\mathbf{s}}, r_z)$ to represent. The Fourier transform of $T'_{\text{b}}(\hat{\mathbf{s}}, r_z)$ is

$$\delta \tilde{T}'(\hat{\mathbf{s}}, k_{\parallel}) = \int \delta T'_{\text{b}}(\hat{\mathbf{s}}, r_z) e^{-ik_{\parallel}r_z} dr_z. \quad (5)$$

The 1D power spectrum along the line of sight is defined as

$$P(\hat{\mathbf{s}}, k_{\parallel}) = \left| \delta \tilde{T}'(\hat{\mathbf{s}}, k_{\parallel}) \right|^2 \left(\frac{1}{\Delta r_z} \right). \quad (6)$$

Here $1/\Delta r_z$ is the normalization factor, where Δr_z is the line of sight length considered. To reveal the small-scale structures we are interested in, we select $\Delta r_z = 10$ comoving Mpc neutral patches

and calculate the 1D power spectrum of the 10 comoving Mpc segment along the line of sight. For a reasonable number $\mathcal{O}(10)$ high- z background sources, the expected value of the 1D power spectrum is obtained by incoherently averaging over 100 neutral patches on the line of sight penetrating various environments, i.e. $P(k_{\parallel}) \equiv \langle P(\hat{s}, k_{\parallel}) \rangle$. In the rest of this work, we abbreviate k_{\parallel} to k because here we are always interested in k along the line of sight. We calculated the 1D power spectrum as presented in Supplementary Fig. 6 of the 21-cm forest corresponding to different conditions. The dotted line indicates the thermal noise of SKA2-LOW when the integration time is 200 hr. It can be seen that using the 1D power spectrum can improve the sensitivity of detecting 21-cm forest signals.

Dataset settings. We finally obtained the simulated correspondence between parameters ($m_{\text{WDM}}, T_{\text{K}}$) and the 1D power spectrum in the presence of thermal noise. Specifically, we simulated 7 simulation boxes with DM particle masses ranging from 3 keV to 9 keV at equal intervals (1 keV). For the gas temperature, we consider two situations. When the heating effect is weak ($f_{\text{X}} \approx 0.1$), the IGM will be heated to about 60 K at $z = 9$. Therefore, we choose equal intervals (5 K) between 40 K and 80 K. When the heating effect is strong ($f_{\text{X}} \approx 1$), the IGM will be heated to about 600 K at $z = 9$. Therefore, we choose equal intervals (100 K) between 400 K and 800 K. In addition, we also generated some data sets of other parameters for validation and test sets. To avoid the influence of the edge effect, we only select the synthetic spectrum of 30×300 in each simulation box to calculate the 1D power spectrum. It should be noted that this method is not limited to the above parameter range and is also applicable to other parameter ranges.

To fit the input parameters to the deep learning model, we first need to normalize the 1D power spectrum and parameters before training and testing the network. For the parameters, we perform normalization as the formula

$$\tilde{\xi} = 2 \frac{\xi - \xi_{\max}}{\xi_{\max} - \xi_{\min}} - 1, \quad (7)$$

where ξ represents the original parameter (m_{WDM} or T_{K}), ξ_{\max} is the maximum value of ξ , and ξ_{\min} is the minimum value of ξ . Due to the significantly higher values of the power spectrum near the halo center, we used logarithmic normalization. This method helps handle the wide range of values and the outliers, ensuring more uniform analysis across different scales. We perform logarithmic normalization on the 1D power spectrum as the formula

$$\tilde{P}(k) = 2 \frac{\log P(k) - \log P_{\max}(k)}{\log P_{\max}(k) - \log P_{\min}(k)} - 1, \quad (8)$$

where $P(k)$ represents the value of the 1D power spectrum at a specific wavenumber k after binning, $\log P_{\max}(k)$ is the logarithm of the maximum 1D power spectrum value at k , and $\log P_{\min}(k)$ is the logarithm of the minimum 1D power spectrum value at k . This approach helps balance the contributions of each scale and improves the stability and efficiency of network training. The data set generated and processed by the above method as presented in Supplementary Fig. 10, which not only provides a solid foundation for training and testing our deep learning model but also ensures the reliability and scientific significance of the research results.

The principle of the normalizing flow. Based on the above simulation, we propose a parameter inference method. The basic idea is to generate a large number of simulated data sets with relevant parameters and use these data sets to train a neural network called the NF²⁰ to approximate

the posterior. By leveraging these simulated data sets, the trained network can quickly generate new posterior samples when observational data is obtained and tested. This bypasses the need to generate the 1D power spectrum at inference time, thereby amortizing expensive training costs across all future detections. The general method for building such models is called neural posterior estimation (NPE)⁶⁵.

In more detail, the NF is a method of probabilistic modeling using deep learning technology. Here, we use the notation of the INF for explanation. The differences between the INF and GNF, as shown in the Fig. 2, are merely the conditions and outputs. The core idea of NFs is to construct a reversible transformation f_P based on the 1D power spectrum P , thereby obtaining the mapping relationship between a simple base distribution (e.g., a normal distribution) and a complex posterior distribution. It is a reversible neural network characterized by the ability to accurately calculate the Jacobian of the probability density function through network transformation. The NF can be mathematically expressed as²⁰

$$Q(\xi|P) = \pi(f_P^{-1}(\xi)) |\det J_{f_P}^{-1}|, \quad (9)$$

where $Q(\xi|P)$ represents the approximate posterior distribution exported by the NF, $\pi(u)$ is typically chosen to be a standard multivariate normal distribution for ease of sampling and density evaluation, and f_P represents the transformation applied to the data. This transformation can be applied iteratively to construct complex densities:

$$f_P(u) = f_{P, N} \circ f_{P, N-1} \circ \cdots \circ f_{P, 1}(u), \quad (10)$$

where each $f_{P, i}(u)$ represents a block of the NF. This iterative approach is central to NPE, where

the goal is to train a parameter conditional distribution that approximates the true posterior distribution. This task translates into an optimization problem aimed at minimizing the expected Kullback-Leibler divergence (KLD) between the true and approximate posterior distributions⁶⁶:

$$\text{KLD}(\mathcal{P} \parallel \mathcal{Q}) = \int_{-\infty}^{+\infty} \mathcal{P}(\xi) \log \frac{\mathcal{P}(\xi)}{\mathcal{Q}(\xi)} d\xi, \quad (11)$$

where $\mathcal{P}(\xi)$ represents the true posterior distribution and $\mathcal{Q}(\xi)$ represents the approximate posterior distribution.

The training of the NF involves minimizing the loss function, which is the expected value of the cross-entropy between the true and model distributions⁶⁷:

$$L = E_{\mathcal{P}(P)} [\text{KLD}(\mathcal{P}(\xi|P) \parallel \mathcal{Q}(\xi|P))]. \quad (12)$$

For a minibatch of training data of size N , this can be approximated as

$$L \approx -\frac{1}{N} \sum_{i=1}^N \log \mathcal{Q}(\xi^{(i)} | P^{(i)}). \quad (13)$$

Our NF is neural spline flow (NSF)⁶⁸, specifically a rational-quadratic neural spline flow with autoregressive layers, RQ-NSF (AR). Each flow is connected by a series of autoregressive layers that share parameters. Specifically, the network uses the conditional and partial vector output from the previous flow (when i is equal to 0, specifically the vector to be sampled from a standard distribution) as the input of a multilayer perceptron (MLP), and uses the output result as an RQ-NSF (AR). These parameters are defined as the width and height of K bins, which ultimately form $K + 1$ knots $\{(x^{(i)}, y^{(i)})\}_{i=0}^K$. The left and right endpoints are $(-B, -B)$ and (B, B) , respectively,

and there are $K - 1$ derivatives of knots $\{y^{(i)}\}_{i=1}^{K-1}$, where the derivatives of the left and right endpoints are set to 1. Therefore, the data is divided into K bins from $-B$ to B . Each stream is a map that maps $-B$ to B and then $-B$ to B again, so the y-axis is also divided into K bins from $-B$ to B . The figure 1 in Ref.⁶⁸ defines the mapping relationship of the coupling transformation when K is 10.

Neural network architecture. NFs, unlike Bayesian methods, do not require an explicit definition of the likelihood function. It employs a likelihood-free approach, making it suitable for handling non-Gaussian data, where deriving an analytical likelihood is either computationally expensive or infeasible. Since the scale of the 21-cm forest is extremely small, generating the 1D power spectra of the 21-cm forest corresponding to a set of parameter points requires very high computational resources. This will make it difficult to obtain 1D power spectrum for any parameter, leading to incorrect estimates of the posterior distribution as presented in Supplementary Fig. 1. Therefore, our method consists of a GNF for generating the 1D power spectrum of arbitrary parameters and an INF for parameter inference. For the GNF, the conditions and outputs correspond to parameters and power spectra, respectively, whereas for the INF, the conditions and outputs correspond to power spectra and parameters, respectively. All the NF networks were trained using the ‘‘Xavier’’⁶⁹ initialization for network parameters and the AdamW optimizer⁷⁰ on a single NVIDIA GeForce RTX A6000 GPU with 48 GB of memory.

The GNF is used to generate a 1D power spectrum corresponding to all parameters in the parameter space. Specifically, the GNF takes a parameter vector as input and finally outputs an

estimate of the 1D power spectrum of the 21-cm forest. It selects 29×300 from the black point data as the training set as presented in Supplementary Fig. 10, the blue point data as the verification set, and the red point as the test set. For GNFs, to prevent overfitting and achieve convergence, we employed early stopping with 15 epochs and utilized L_2 regularization⁷¹. For both weaker and stronger heating effects, the activation function we used is rectified linear units (ReLU), the size of the hidden layers is 256, the number of bins is 8, the batch size is 256, the learning rate decay factor is 0.99, and L_2 regularization is set to 0.0001. The only difference is that for the weaker heating effect, the flow steps and transform blocks are both 8, and the learning rate is 0.0001, whereas for the stronger heating effect, the flow steps and transform blocks are both 6 and the learning rate is 0.0002.

The INF is designed to perform parameter reasoning based on data generated by the GNF. For the INF, its architecture is similar to the GNF. If the GNF can perfectly grasp the characteristics of the 1D power spectrum, then using the sampling points of the GNF within the prior range as the input of the INF, the INF can obtain appropriate inference results for the simulation data. For the INF, to ensure it adequately captures the posterior distribution of parameters, we employed 250 training epochs. For both weaker and stronger heating effects, the activation function we used is ReLU, the number of bins is 8, the flow steps and transform blocks are both 6, the batch size is 256, the learning rate decay factor is 0.99, and the learning rate is 0.0002. The only difference is that for the weaker heating effect, the size of the hidden layers is 128, whereas for the stronger heating effect, the size of the hidden layers is 256. Therefore, it receives the 1D power spectrum generated by the GNF as input during training to map it into a standard distribution. This enables

simulation-based parameter estimation during testing. It selects the 1D power spectra generated by the GNF as the training set and trains for 300 epochs to ensure sufficient fitting. The remaining 300 in the black point data is used as the test set as presented in Supplementary Fig. 10.

Model evaluation method. We use the coefficient of determination of mean and standard deviation to test whether the 1D power spectrum generated by the GNF is reasonable, respectively. its expression is

$$R^2 = 1 - \frac{\sum(y_{\text{pred}} - y)^2}{\sum(y - \bar{y})^2}, \quad (14)$$

where y_{pred} and y represent the mean value or standard deviation of the 1D power spectra generated by the GNF and the 1D power spectra corresponding to different scales generated by simulation, respectively. \bar{y} represents the mean or standard deviation of the simulated generated 1D power spectra on different scales. To check whether the generated distribution under different conditions and different scales is consistent with the simulated situation, its JSD is also calculated by

$$\text{JSD}(\mathcal{P}_{\text{sim}} \parallel \mathcal{Q}_{\text{gen}}) = \frac{1}{2}\text{KLD}(\mathcal{P}_{\text{sim}} \parallel \frac{\mathcal{P}_{\text{sim}} + \mathcal{Q}_{\text{gen}}}{2}) + \frac{1}{2}\text{KLD}(\mathcal{Q}_{\text{gen}} \parallel \frac{\mathcal{P}_{\text{sim}} + \mathcal{Q}_{\text{gen}}}{2}), \quad (15)$$

where \mathcal{P}_{sim} and \mathcal{Q}_{gen} represent the distribution of simulated 1D power spectra and the GNF-generated 1D power spectra on different k , respectively. The JSD is a symmetric measure of similarity between two probability distributions. A smaller JSD value indicates a higher degree of similarity between the distributions, effectively addressing the asymmetry issue inherent in KLD.

To evaluate the distribution characteristics of the 1D power spectra of the 21-cm forest on a specific scale under different astrophysical conditions, we used the skewness coefficient in statistical analysis as a key indicator to measure its Gaussianity. We calculated the skewness coefficient

of the normalized 1D power spectrum at different scales k , which is defined as the cubic ratio of the third-order normalized moment to the standard deviation:

$$S = E \left(\frac{P(k) - \mu}{\sigma} \right)^3, \quad (16)$$

where $P(k)$ represents the normalized 1D power spectrum at different scales k , μ is the mean value of $P(k)$, σ is the standard deviation of $P(k)$, and E represents the expected value. If the value of S is close to zero, then it can be considered to be symmetrical on that scale and close to a Gaussian distribution. If S is significantly different from zero, it indicates that the distribution has an obvious skew.

To quantify the correlation between different scales k of the 1D power spectrum of the 21-cm forest, we use the Spearman correlation coefficient⁷². The Spearman correlation coefficient is a non-parametric measure of rank correlation that assesses the monotonic relationship between two variables. It does not assume a normal distribution of the data, making it more robust for handling non-Gaussian distributions. Given the significant non-Gaussian characteristics of our data, we chose the Spearman correlation coefficient to more accurately capture the correlations between different scales. This approach helps avoid errors that could arise from assuming a Gaussian distribution of the data. If all n ranks are distinct integers, the Spearman correlation coefficient ρ is defined as

$$\rho = 1 - \frac{6 \sum d_i^2}{n(n^2 - 1)}, \quad (17)$$

where d_i is the difference between the ranks of corresponding values of the two variables, and n is the number of observations.

In our analysis, we employ the KS test³⁹ to assess the fit between the posterior distribution of the INF's output and the theoretical distribution. The KS test compares the empirical distribution derived from the sample data with a specified theoretical distribution by measuring the maximum difference between their CDFs. This difference is known as the KS statistic d , which can be expressed as

$$d = \max |F_n(x) - F(x)|, \quad (18)$$

where $F_n(x)$ is the empirical CDF of the sample, $F(x)$ is the theoretical CDF. Theoretically, within a given confidence interval of the posterior distribution, the percentage of actual data should match the confidence level. Therefore, the theoretical CDF should be uniform. To interpret the d value in terms of statistical significance, we calculate a p -value using the distribution of the KS statistic under the null hypothesis. This p -value represents the probability of observing a KS statistic as extreme as d , assuming that the sample distribution is drawn from the theoretical distribution. The CDF of the KS statistic under the null hypothesis is given by

$$Q(d) = 2 \sum_{i=1}^{\infty} (-1)^{i-1} e^{-2i^2 d^2}. \quad (19)$$

The p -value is derived from this function and represents the probability of observing a value as extreme as the calculated d . A small p -value (typically indicated by a significance level of 0.05) would lead us to reject the null hypothesis, suggesting a significant discrepancy between the empirical and theoretical distributions.

Data Availability All datasets are available from the corresponding authors upon reasonable request.

Code Availability The code 21cmFAST used for large-scale simulation is publicly available at <https://github.com/andreimesinger/21cmFAST>, the codes for simulating small-scale structures and 21-cm forest signals are available from the corresponding authors upon reasonable request. The code for building deep learning networks is publicly available at <https://github.com/probabilists/lampe>, and the codes for training and testing in deep learning are available from the corresponding authors upon reasonable request.

Additional information **Correspondence and requests for materials** should be addressed to Xin Zhang (email: zhangxin@mail.neu.edu.cn).

Acknowledgements This work was supported by the National SKA Program of China (Grants Nos. 2022SKA0110200 and 2022SKA0110203), the National Natural Science Foundation of China (Grants Nos. 11975072, 11875102, and 11835009), and the National 111 Project (Grant No. B16009).

Author contributions Tian-Yang Sun performed most of the computation and wrote the majority of the manuscript. Yue Shao performed part of the computation and wrote part of the manuscript. Yichao Li and Yidong Xu wrote part of the manuscript. Xin Zhang and Yidong Xu proposed the study. Xin Zhang led the study and contributed to the manuscript writing. All authors discussed the results and commented on the manuscript.

Competing Interests The authors declare no competing interests.

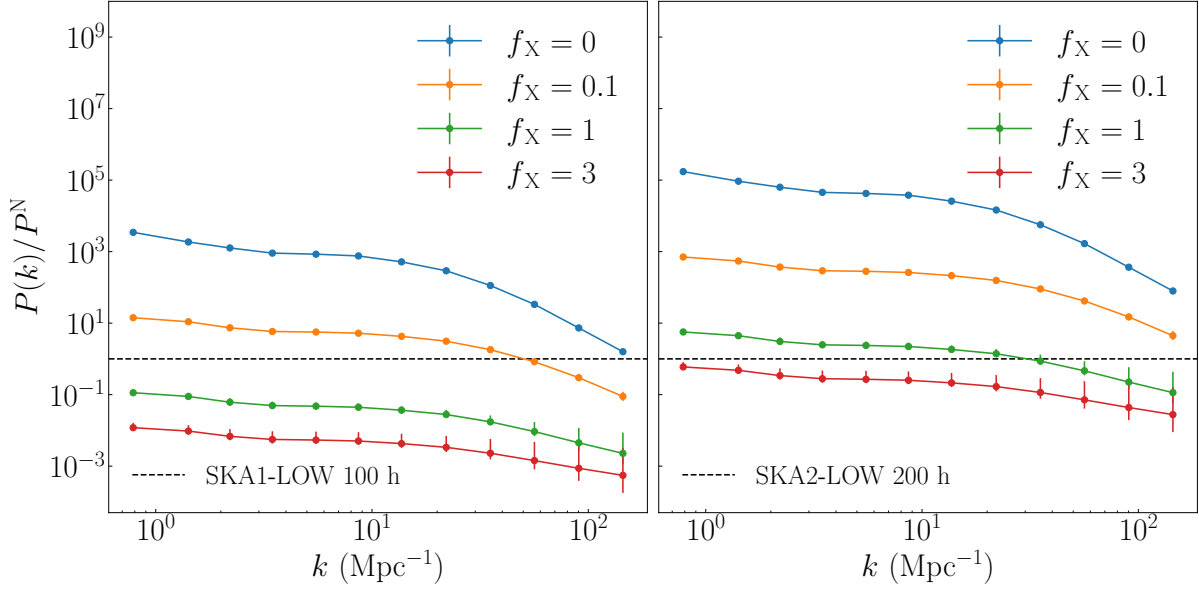


Figure 1 | The SNR of the 1D power spectrum of the 21-cm forest corresponding to different heating levels in the WDM model with $m_{\text{WDM}} = 6$ keV. The blue, orange, green and red curves correspond to $f_X = 0$, $f_X = 0.1$, $f_X = 1$ and $f_X = 3$, respectively. The left panel presents the SNR with an integration time of 100 h on each source using SKA1-LOW, and the right panel presents the results for an integration time of 200 h on each source using SKA2-LOW. The error bars show the sample variances of the 1D power spectra of the 21-cm forest. The black dashed line in each panel indicates the SNR of 1.

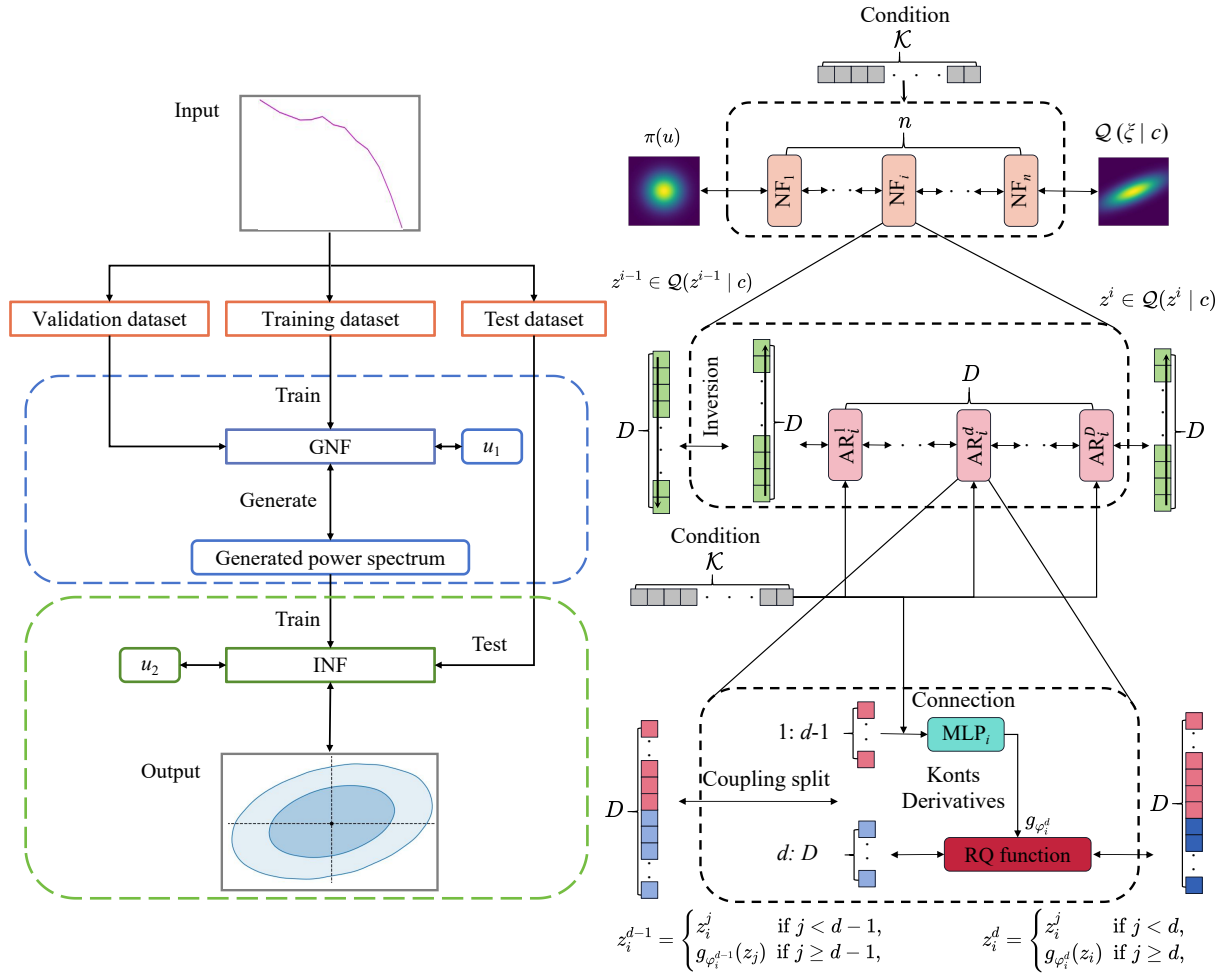


Figure 2 | Network workflow chart (left panel) and schematic diagram of the architecture of the NF (right panel). Both the GNF and INF are composed of RQ-NSF (AR). In the GNF, the conditions are parameters, and the output is a 1D power spectrum. Conversely, in the INF, the condition is a 1D power spectrum, and the outputs are parameters. The network consists of a sequence of flows, each of which consists of a sequence of autoregressive layers that share parameters. Input the condition and the sampling vector obtained from the base distribution into the NFs to generate the output. The simulated power spectra data set is divided into a training set, a validation set, and a test set. The

training set and validation set are used to train the GNF, which generates reasonable power spectra for any given parameters. The INF is trained using the 1D power spectra generated by the GNF to learn the parameter distribution corresponding to any given power spectrum. Different test sets of simulated power spectra are used to verify the rationality of the GNF and the INF, respectively.

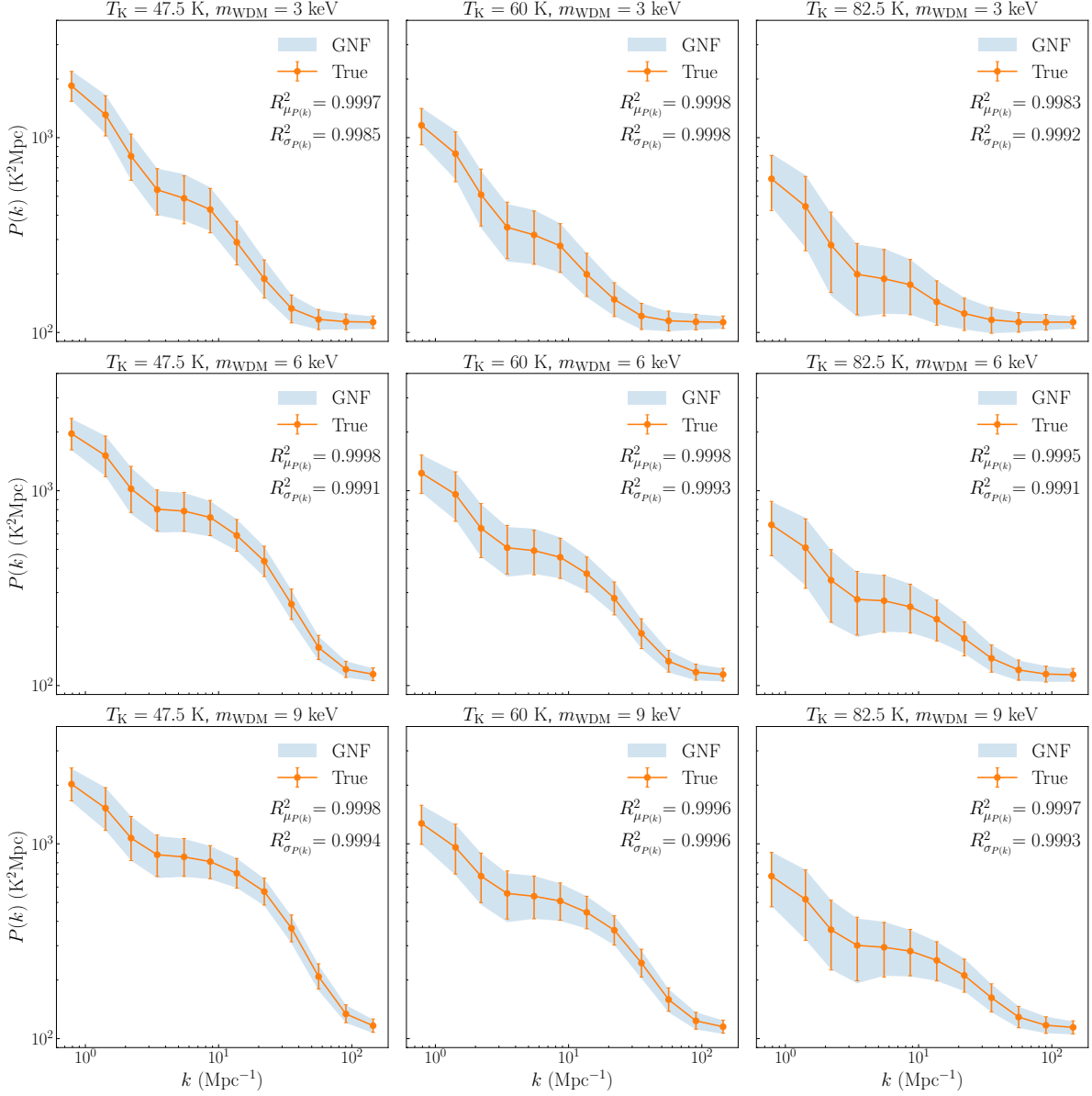


Figure 3 | The mean value and 1σ distribution diagram of the GNF-generated 1D power spectra and simulated 1D power spectra corresponding to different T_K and m_{WDM} with an integration time of 100 h using SKA1-LOW. The blue area is the 1σ range of the 1D power spectrum generated by the GNF. The orange line and bar are the mean and 1σ error bar of the simulated power spectrum. $R^2_{\mu_{P(k)}}$ and $R^2_{\sigma_{P(k)}}$ are the correlation coefficients of the mean and standard deviation, respectively.

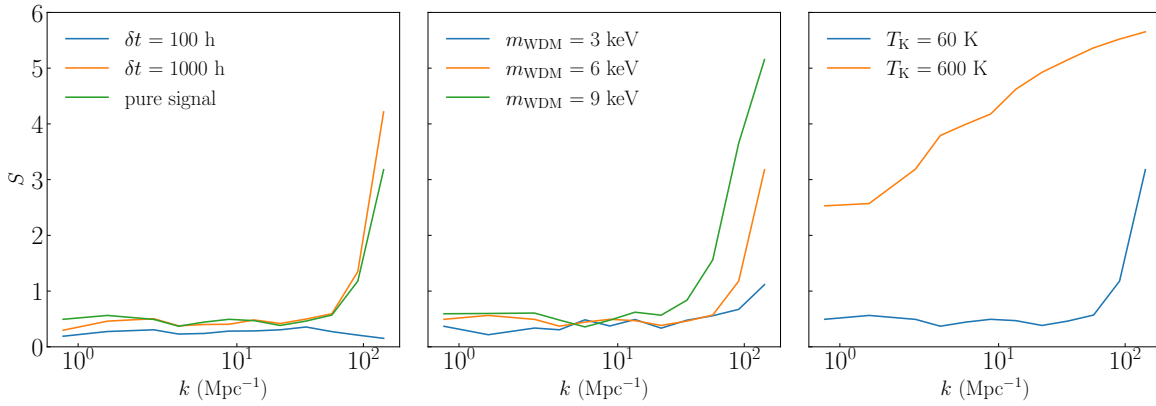


Figure 4 | S of the 1D power spectrum at different integration time, m_{WDM} , and T_{K} . The blue, orange, and green curves in the left panel present the S of the 1D power spectrum at different k when $m_{\text{WDM}} = 6$ keV and $T_{\text{K}} = 60$ K, and the SKA1-LOW integration time is 100 h, 1000 h, and infinity (pure signal), respectively. The blue, orange, and green curves in the middle panel present the S of the 1D power spectrum at different k when $T_{\text{K}} = 60$ K, and m_{WDM} is 3 keV, 6 keV, and 9 keV, respectively. The blue and orange curves in the right panel present the 1D power spectrum S of the pure signal at different k when $m_{\text{WDM}} = 6$ keV and T_{K} is 60 K and 600 K, respectively.

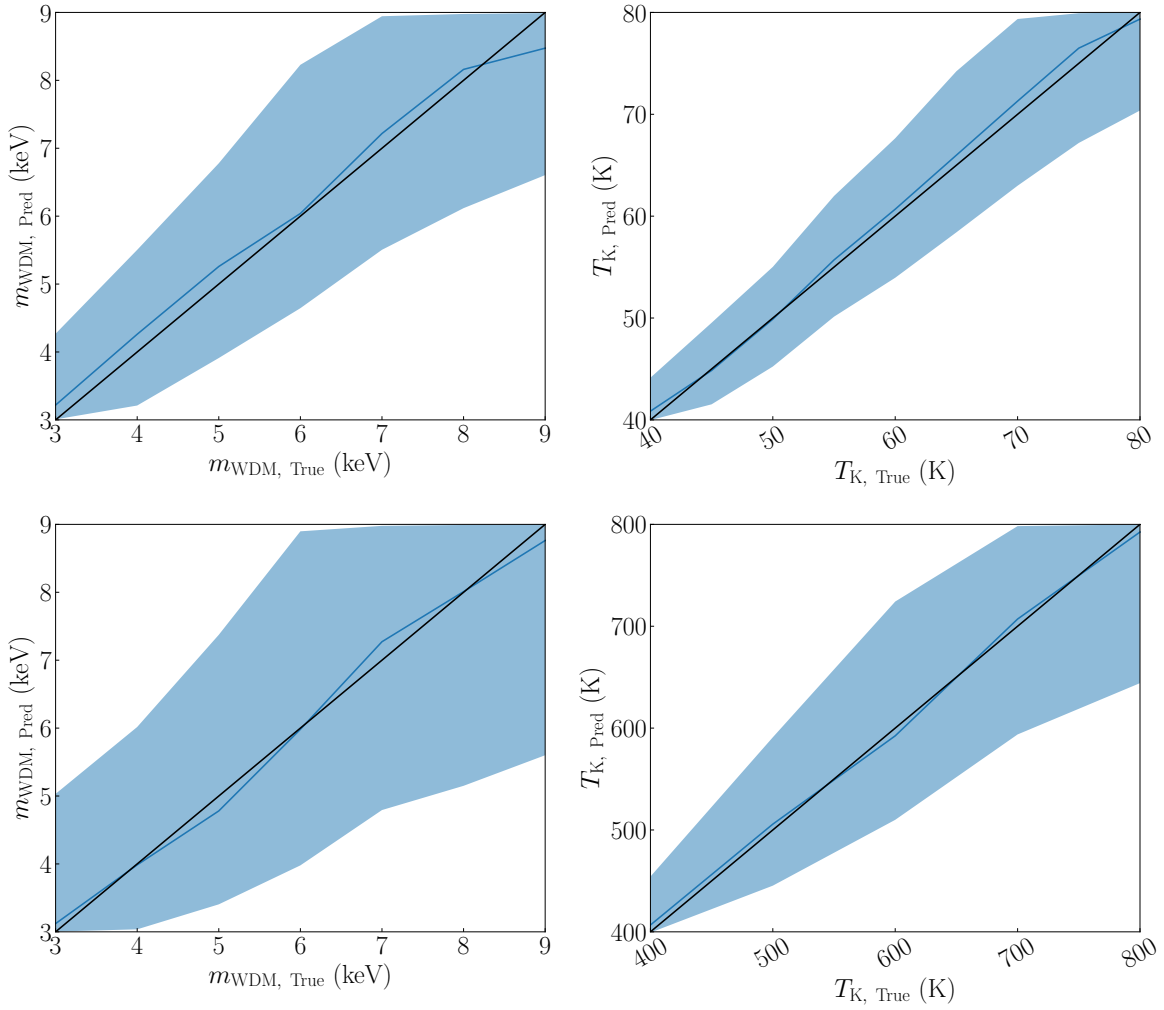


Figure 5 | The inference results for m_{WDM} and T_{K} of the INF. The blue line represents the most probable values under different parameters, and the blue area indicates the 1σ confidence interval. The value corresponding to each parameter is the average of the results of all test data under this parameter. The black diagonal line represents perfect (zero-error) results. The upper and lower panels present the constrained results of parameters using SKA1-LOW and SKA2-LOW, respectively. The left panels represent the predicted value ξ_{Pred} and the true value ξ for m_{WDM} , while the right panels show these values for T_{K} .

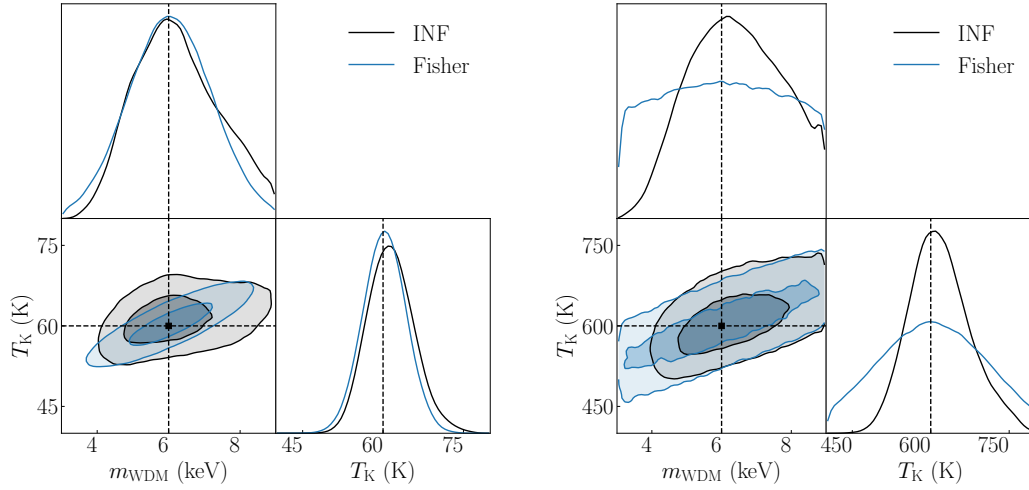
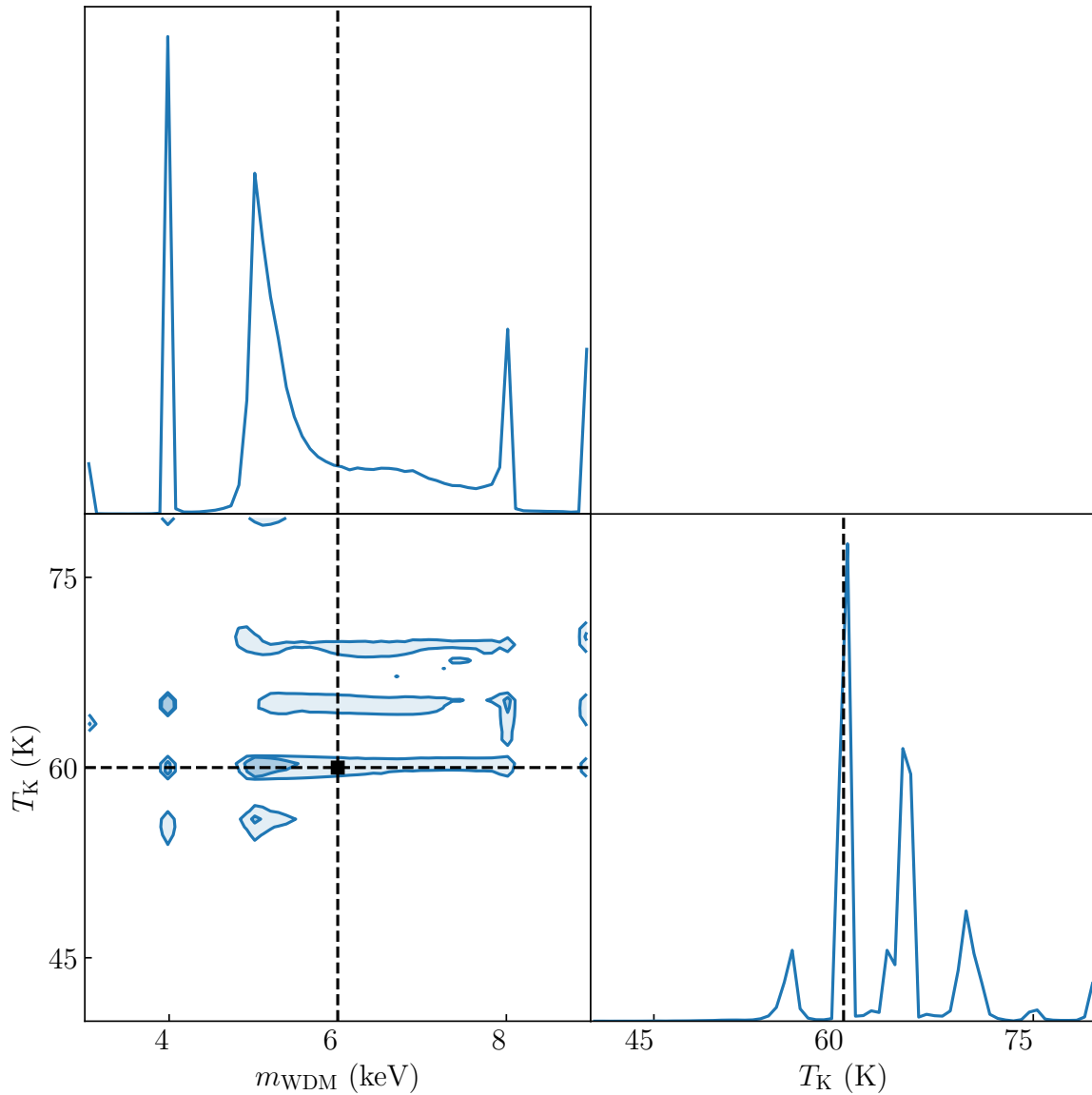
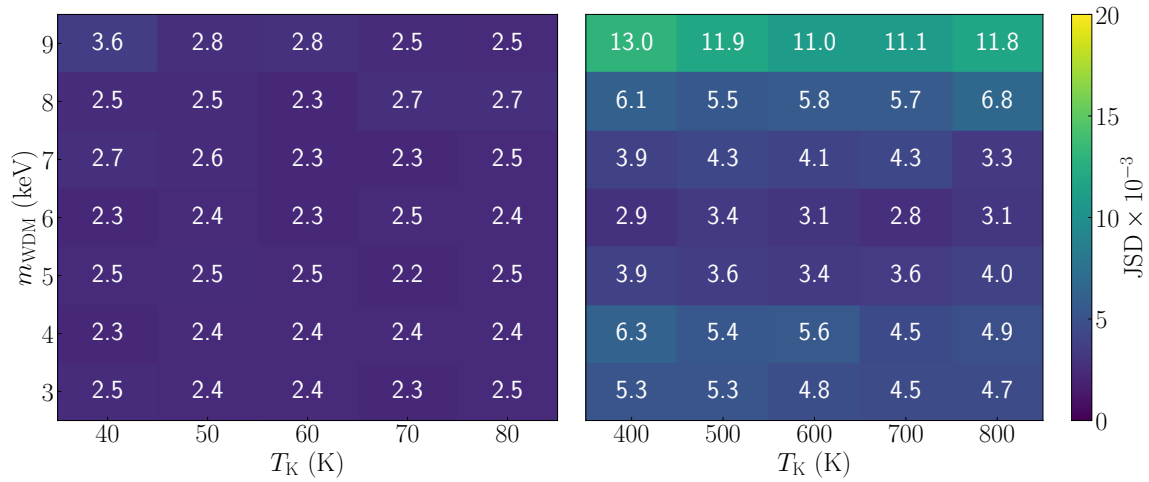


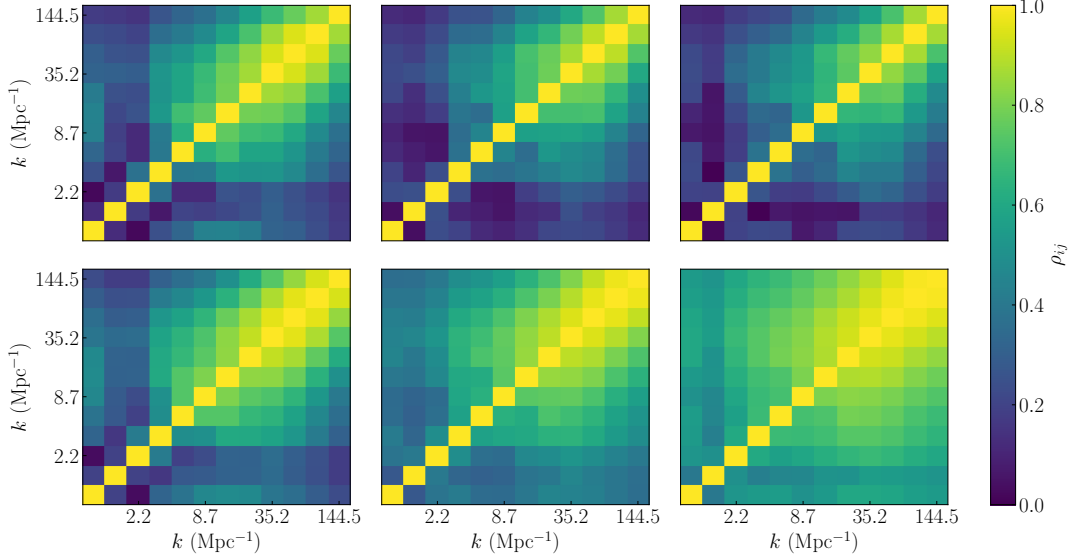
Figure 6 | Constraints on m_{WDM} and T_{K} with the INF and Fisher matrix. The black contour is based on the INF and the blue contour is based on the Fisher matrix. The left panel presents the results when $m_{\text{WDM}} = 6$ keV and $T_{\text{K}} = 60$ K with an integration time of 100 h using SKA1-LOW. The right panel presents the results when $m_{\text{WDM}} = 6$ keV and $T_{\text{K}} = 600$ K with an integration time of 200 h using SKA2-LOW. Contours represent 1σ and 2σ confidence intervals.



Supplementary Figure 1 | The resulting diagram of parameter inference using the NF directly without the INF for data enhancement. Due to the missing part of the 1D power spectrum corresponding to the parameters, the NF cannot obtain reasonable parameter inference results. The panel presents the results when $m_{\text{WDM}} = 6$ keV and $T_{\text{K}} = 60$ K with an integration time of 100 h using SKA1-LOW. Contours represent 1σ and 2σ confidence intervals.



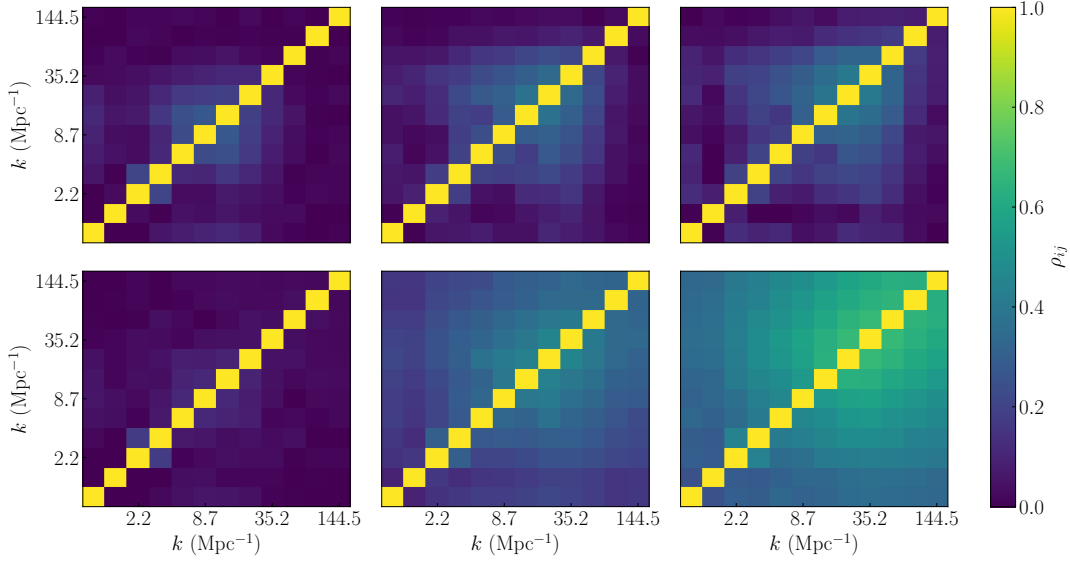
Supplementary Figure 2 | JSDs between GNF and simulated power spectra at different T_K and m_{WDM} . The left panel presents the average JSDs of the 1D power spectra generated by different parameters at different k with an SKA1-LOW integration time of 100 h in the case of a weaker heating effect. The right panel presents the average JSDs of the power spectra generated by different parameters at different k with an SKA2-LOW integration time of 200 h in the case of a stronger heating effect.



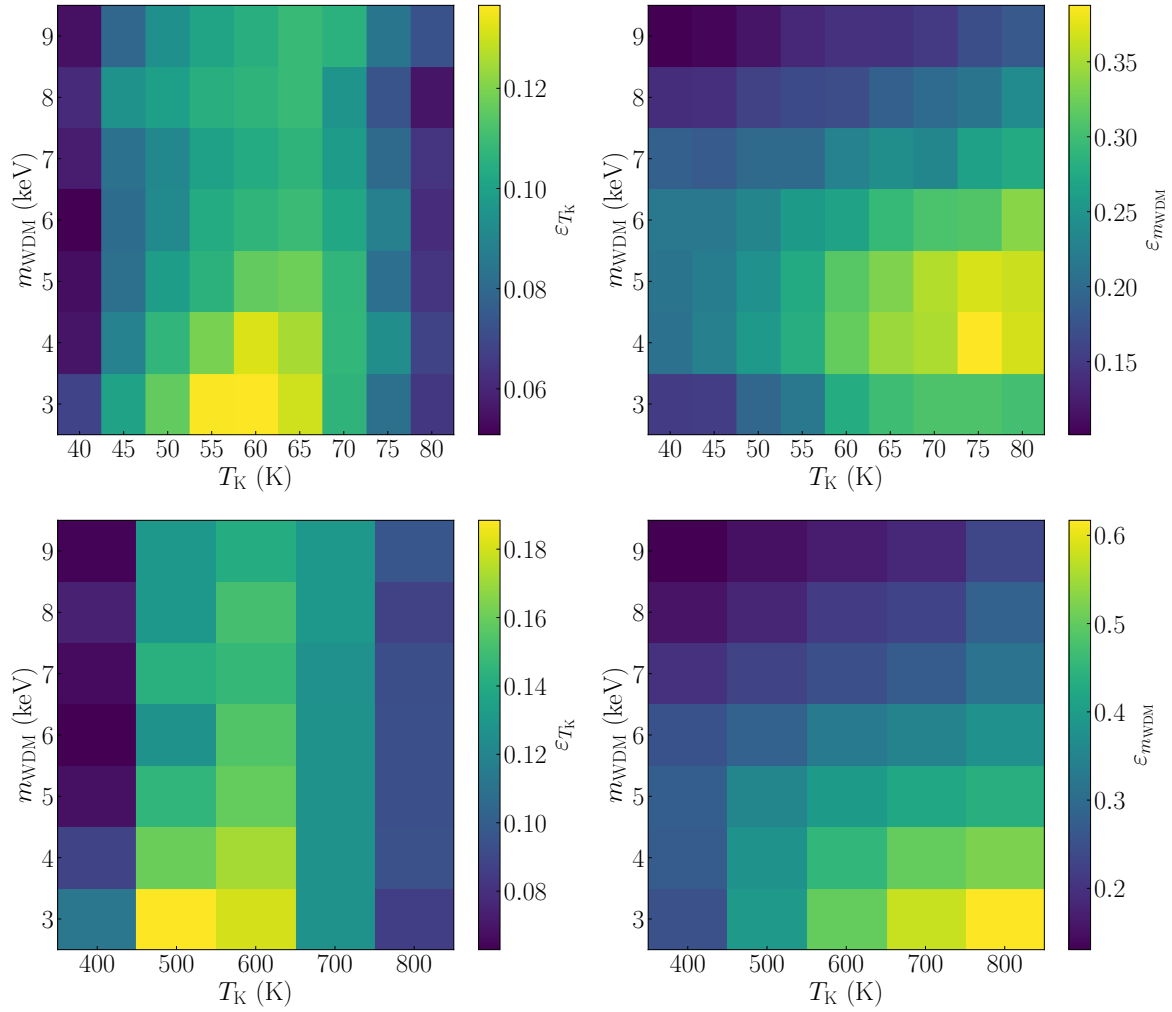
Supplementary Figure 3 | The spearman correlation coefficient ρ_{ij} estimated from the 1D power spectrum of 21-cm forest at $z = 9$ without considering thermal noise.

The upper and lower panels present ρ_{ij} estimated from the 1D power spectrum of 21-cm forest with weaker ($T_K = 60$ K) and stronger ($T_K = 600$ K) heating effects, respectively.

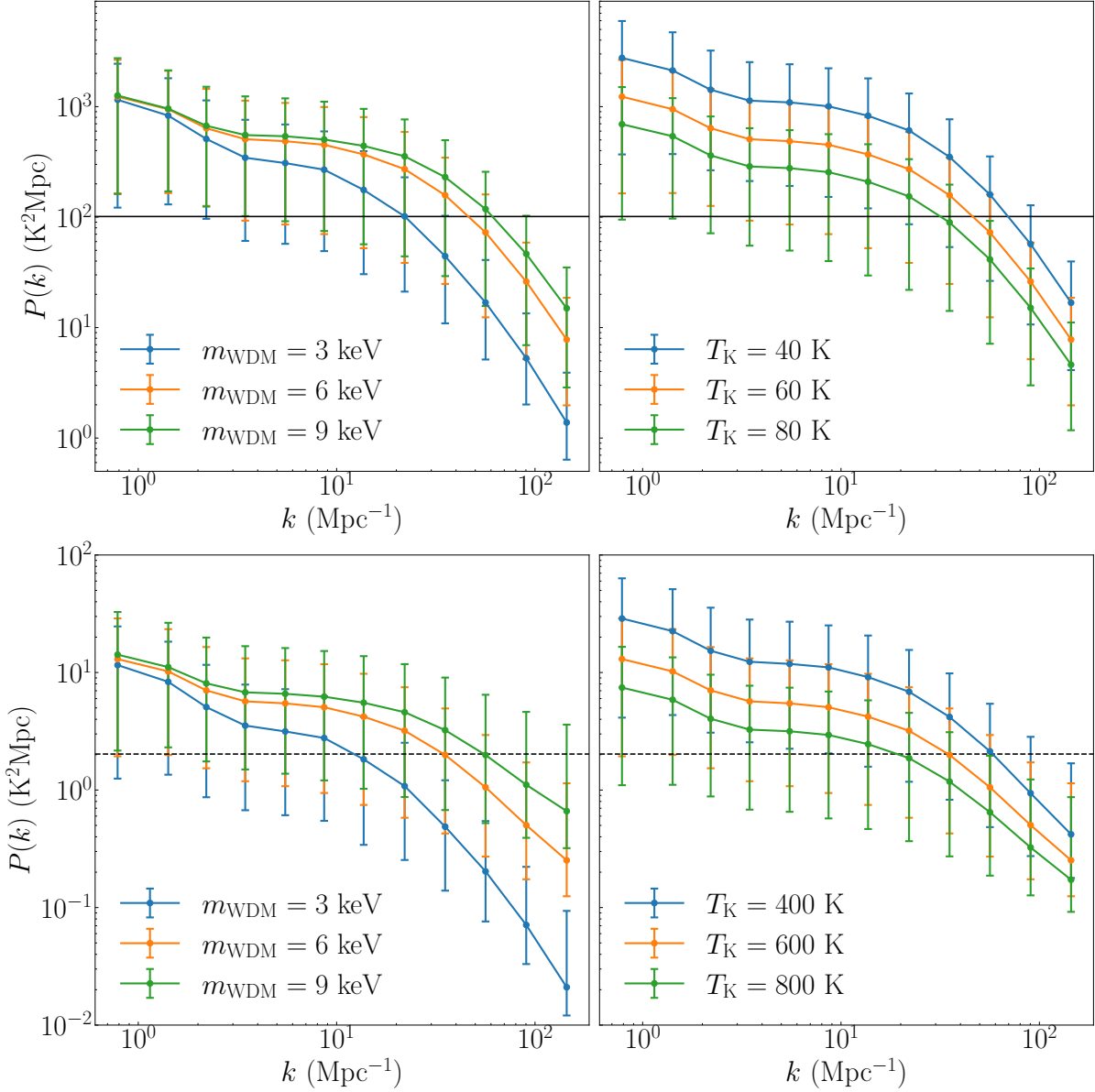
The left, middle, and right panels present ρ_{ij} estimated from the 1D power spectrum of 21-cm forest with $m_{\text{WDM}} = 3$ keV, $m_{\text{WDM}} = 6$ keV and $m_{\text{WDM}} = 9$ keV, respectively.



Supplementary Figure 4 | The spearman correlation coefficient ρ_{ij} estimated from the 1D power spectrum of 21-cm forest at $z = 9$ with thermal noise. The upper and lower panels present ρ_{ij} estimated from the 1D power spectrum of 21-cm forest with for weaker ($T_K = 60$ K with an integration time of 100 h using SKA1-LOW) and stronger ($T_K = 600$ K with an integration time of 200 h using SKA2-LOW) heating effects, respectively. The left, middle, and right panels present ρ_{ij} estimated from the 1D power spectrum of 21-cm forest with $m_{\text{WDM}} = 3$ keV, $m_{\text{WDM}} = 6$ keV and $m_{\text{WDM}} = 9$ keV, respectively.

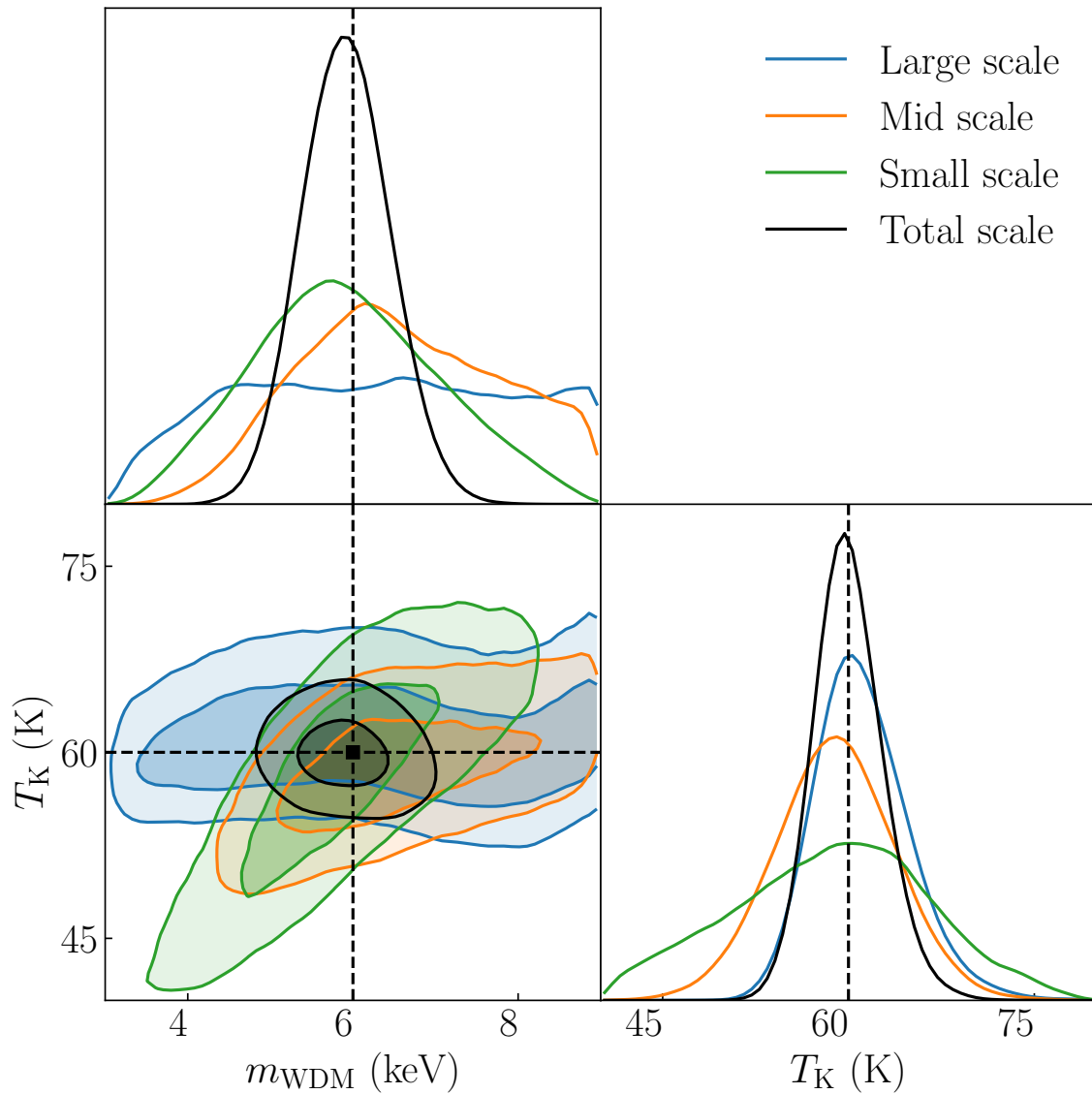


Supplementary Figure 5 | Precision distribution of parameter constrains for the INF for different T_K and m_{WDM} . The upper left panel and lower left panel present the temperature constrained precision of the T_K using SKA1-LOW and SKA2-LOW, respectively. The upper and lower right panels present the constrained precision of m_{WDM} using SKA1-LOW and SKA2-LOW, respectively.



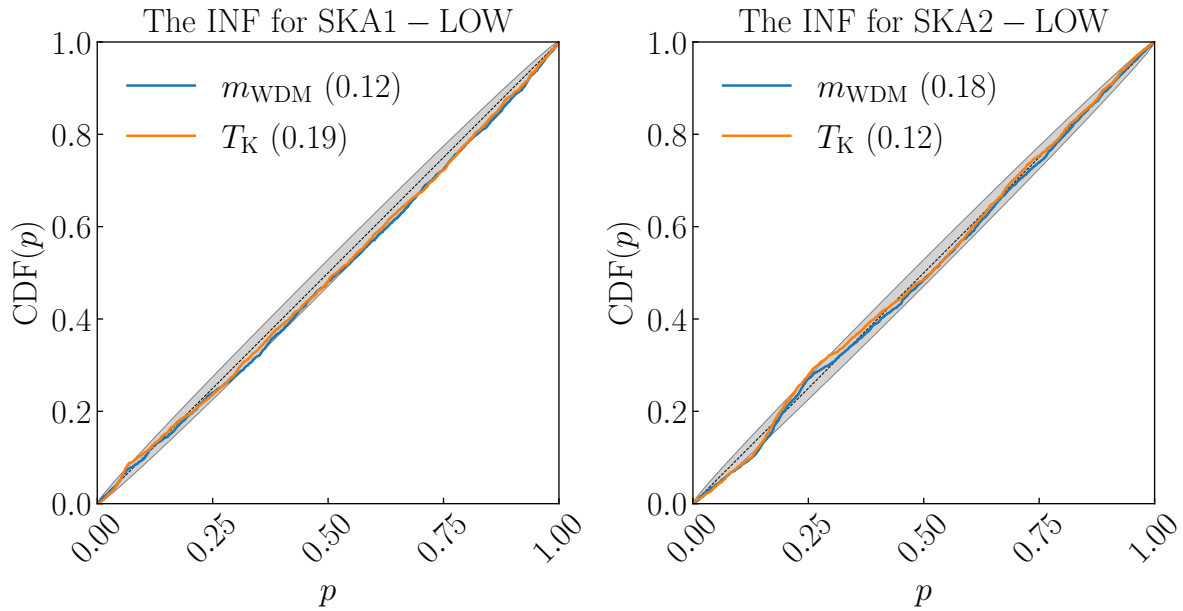
Supplementary Figure 6 | Expected 1D power spectrum of the 21-cm forest. A total of 100 measurements of 10 comoving Mpc length segments along the line-of-sight neutral patch against 10 background light sources with $S_{150} = 10$ mJy yielded the expected value for the 1D power spectrum of 21-cm forest at $z = 9$. The left panels present the 1D power spectra for different m_{WDM} values in the WDM models. Blue, orange, and green correspond to $m_{\text{WDM}} = 3$ keV, $m_{\text{WDM}} = 6$ keV and $m_{\text{WDM}} = 9$ keV, respectively. T_{K} in the

upper left panel are both $T_K = 60$ K, and T_K in the lower left panel are all $T_K = 600$ K. The right panel presents the 1D power spectra corresponding to the different T_K . In all cases, m_{WDM} is set to 6 keV. The blue, orange, and green in the upper right panel correspond to $T_K = 40$ K, $T_K = 60$ K and $T_K = 80$ K. The blue, orange, and green in the lower right panel correspond to $T_K = 400$ K, $T_K = 600$ K and $T_K = 800$ K, respectively. The black solid and dashed lines are the thermal noises P^{N} expected for an integration time of 100 h using SKA1-LOW and an integration time of 200 h using SKA2-LOW, respectively. The error bars show sample variances of the 1D power spectra of the 21-cm forest.

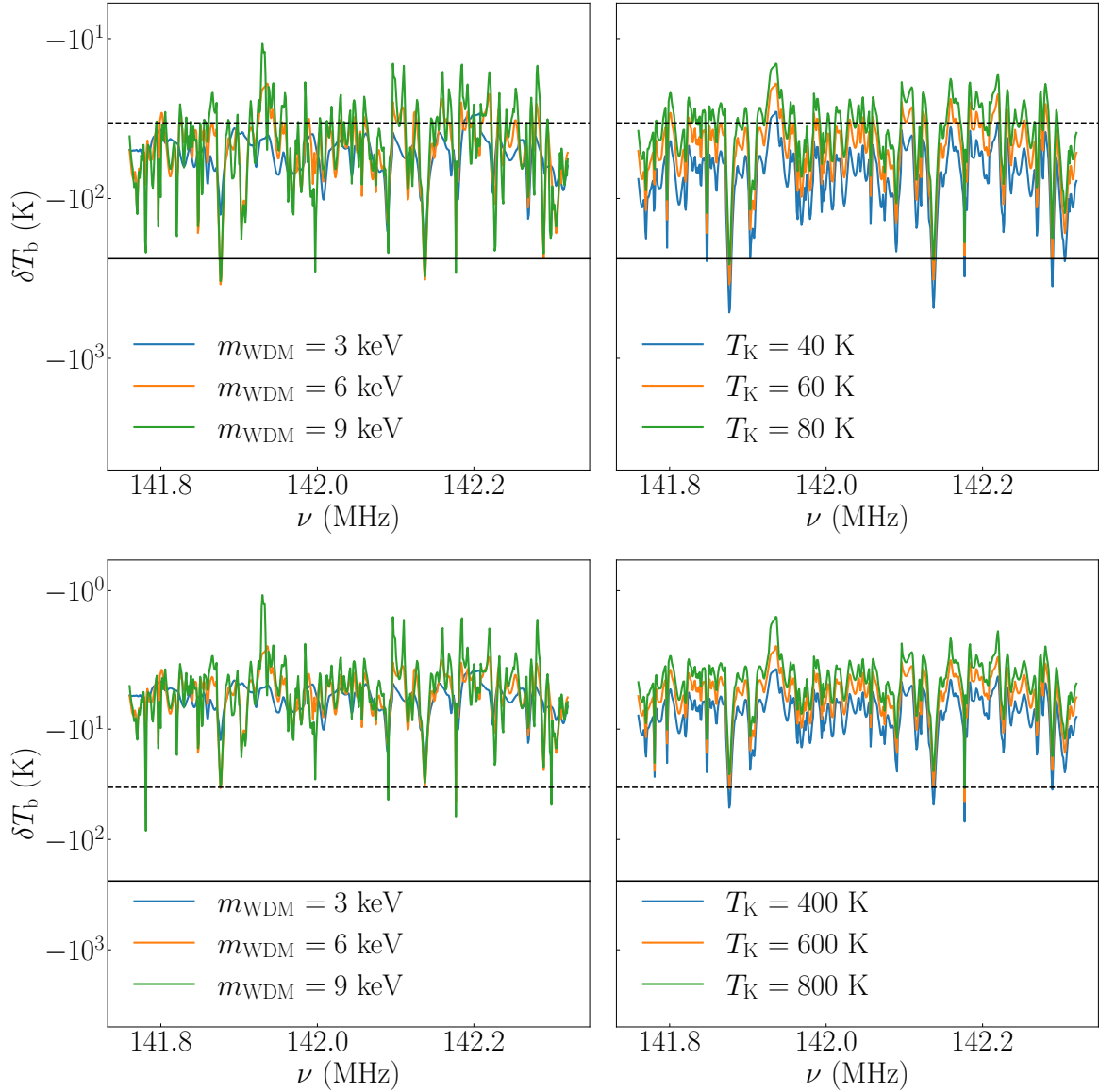


Supplementary Figure 7 | Constraints on m_{WDM} and T_{K} using different scales of 1D power spectra with the INF without considering thermal noise. The blue contour is based on the INF for k in $[0.8 \text{ Mpc}^{-1}, 3.5 \text{ Mpc}^{-1}]$, the green contour is based on the INF for k in $[5.5 \text{ Mpc}^{-1}, 22.0 \text{ Mpc}^{-1}]$, the orange contour is based on the INF for k in $[35.2 \text{ Mpc}^{-1}, 144.5 \text{ Mpc}^{-1}]$ and the black contour is based on the INF for total scale. The panel presents the results when $m_{\text{WDM}} = 6 \text{ keV}$ and $T_{\text{K}} = 60 \text{ K}$ with an integration time of 100 h using

SKA1-LOW.



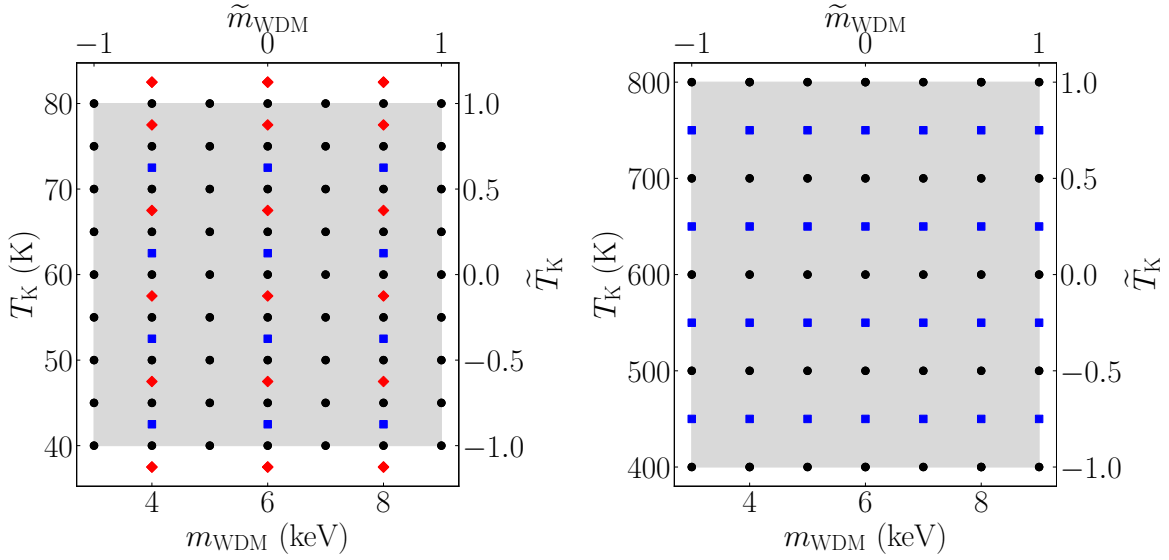
Supplementary Figure 8 | P-P plot of the INF parameter inference. The left panel presents the P-P plot of the INF inference with an integration time of 100 h using SKA1-LOW and for a total of 2700 power spectra with m_{WDM} ranging from 5 keV to 7 keV and T_{K} from 50 K to 70 K. The right panel presents the P-P plot of the INF inference with an integration time of 200 h using SKA2-LOW and for a total of 2700 power spectra with m_{WDM} ranging from 5 keV to 7 keV and T_{K} from 400 K to 800 K. The gray area is the range of the 3σ confidence interval. KS test p -values are denoted in the legend.



Supplementary Figure 9 | Expected brightness temperature of the 21-cm forest. A

total of 10 measurements of 10 comoving megaparsec length segments along a line-of-sight neutral patch against 1 background light source with $S_{150} = 10$ mJy yielded the expected value for the brightness temperature of 21-cm forest at $z = 9$. The left panels present the brightness temperature for different m_{WDM} values in the WDM models. Blue, orange, and green correspond to $m_{\text{WDM}} = 3$ keV, $m_{\text{WDM}} = 6$ keV and $m_{\text{WDM}} = 9$ keV,

respectively. T_K in the upper left panel are both $T_K = 60$ K, and T_K in the lower left panel are all $T_K = 600$ K. The right panels present the brightness temperature corresponding to the different T_K . In all cases, m_{WDM} is set to 6 keV. The blue, orange, and green in the upper right panel correspond to $T_K = 40$ K, $T_K = 60$ K and $T_K = 80$ K. The blue, orange, and green in the lower right panel correspond to $T_K = 400$ K, $T_K = 600$ K and $T_K = 800$ K, respectively. The black solid and dashed lines are thermal noise levels δT^{N} expected for an integration time of 100 h using SKA1-LOW and an integration time of 200 h using SKA2-LOW, respectively.



Supplementary Figure 10 | The parameter ($m_{\text{WDM}}, T_{\text{K}}$) distribution of the simulated data with an integration time of 100 h using SKA1-LOW (left panel) and 200 h using SKA2-LOW (right panel). In the left panel, black, blue and red correspond to the training set, verification set, and test set of the INF, respectively. The normalized parameter ($\tilde{m}_{\text{WDM}}, \tilde{T}_{\text{K}}$) axes are also presented. The test set of the GNF is the untrained part corresponding to the black data set. In the right panel, black and blue correspond to the training set and verification set of the INF, respectively. The test set of the GNF is the untrained part corresponding to the black data set.

1. Carilli, C. L., Gnedin, N. Y. & Owen, F. H I 21 Centimeter Absorption beyond the Epoch of Reionization. *Astrophys. J.* **577**, 22–30 (2002). [astro-ph/0205169](#).
2. Furlanetto, S. & Loeb, A. The 21 cm forest: Radio absorption spectra as a probe of the intergalactic medium before reionization. *Astrophys. J.* **579**, 1–9 (2002). [astro-ph/0206308](#).

3. Furlanetto, S. The 21 Centimeter Forest. *Mon. Not. Roy. Astron. Soc.* **370**, 1867–1875 (2006).
astro-ph/0604223.
4. Xu, Y., Chen, X., Fan, Z., Trac, H. & Cen, R. The 21 cm Forest as a Probe of the Reionization and The Temperature of the Intergalactic Medium. *Astrophys. J.* **704**, 1396–1404 (2009).
0904.4254.
5. Xu, Y., Ferrara, A. & Chen, X. The earliest galaxies seen in 21 cm line absorption. *Mon. Not. Roy. Astron. Soc.* **410**, 2025–2042 (2011). 1009.1149.
6. Ciardi, B. *et al.* Prospects for detecting the 21 cm forest from the diffuse intergalactic medium with LOFAR. *Mon. Not. R. Astron. Soc.* **428**, 1755–1765 (2013). 1209.2615.
7. Bode, P., Ostriker, J. P. & Turok, N. Halo formation in warm dark matter models. *Astrophys. J.* **556**, 93–107 (2001). astro-ph/0010389.
8. Hu, W., Barkana, R. & Gruzinov, A. Cold and fuzzy dark matter. *Phys. Rev. Lett.* **85**, 1158–1161 (2000). astro-ph/0003365.
9. Xu, Y., Ferrara, A., Kitaura, F. S. & Chen, X. Searching for the earliest galaxies in the 21 cm forest. *Science China Physics, Mechanics, and Astronomy* **53**, 1124–1129 (2010).
1002.4356.
10. Shimabukuro, H., Ichiki, K., Inoue, S. & Yokoyama, S. Probing small-scale cosmological fluctuations with the 21 cm forest: Effects of neutrino mass, running spectral index, and warm dark matter. *Phys. Rev. D* **90**, 083003 (2014). 1403.1605.

11. Shao, Y. *et al.* The 21-cm forest as a simultaneous probe of dark matter and cosmic heating history. *Nature Astron.* **7**, 1116–1126 (2023). 2307.04130.
12. Bird, S. *et al.* PRIYA: a new suite of Lyman- α forest simulations for cosmology. *JCAP* **10**, 037 (2023). 2306.05471.
13. Baur, J., Palanque-Delabrouille, N., Yèche, C., Magneville, C. & Viel, M. Lyman-alpha Forests cool Warm Dark Matter. *JCAP* **08**, 012 (2016). 1512.01981.
14. Carilli, C., Gnedin, N. Y. & Owen, F. Hi 21cm absorption beyond the epoch of re-ionization. *Astrophys. J.* **577**, 22–30 (2002). astro-ph/0205169.
15. Mondal, R., Bharadwaj, S. & Majumdar, S. Statistics of the epoch of reionization (EoR) 21-cm signal – II. The evolution of the power-spectrum error-covariance. *Mon. Not. Roy. Astron. Soc.* **464**, 2992–3004 (2017). 1606.03874.
16. Muñoz, J. B. An Effective Model for the Cosmic-Dawn 21-cm Signal (2023). 2302.08506.
17. Press, T. & Teukolsky, S. Vetterling, and flannery. numerical recipes in c (1992).
18. McLachlan, G. & Peel, D. Wiley series in probability and statistics. *Finite Mixture Models* 420–427 (2000).
19. Blei, D. M., Kucukelbir, A. & McAuliffe, J. D. Variational inference: A review for statisticians. *Journal of the American statistical Association* **112**, 859–877 (2017).
20. Rezende, D. & Mohamed, S. Variational inference with normalizing flows. In *International conference on machine learning*, 1530–1538 (PMLR, 2015).

21. Hassan, S. *et al.* HIFlow: Generating Diverse Hi Maps and Inferring Cosmology while Marginalizing over Astrophysics Using Normalizing Flows. *Astrophys. J.* **937**, 83 (2022). 2110.02983.
22. Friedman, R. & Hassan, S. HIGlow: Conditional Normalizing Flows for High-Fidelity HI Map Modeling (2022). 2211.12724.
23. Gillet, N., Mesinger, A., Greig, B., Liu, A. & Ucci, G. Deep learning from 21-cm tomography of the Cosmic Dawn and Reionization. *Mon. Not. Roy. Astron. Soc.* **484**, 282–293 (2019). 1805.02699.
24. Zhao, X., Mao, Y., Cheng, C. & Wandelt, B. D. Simulation-based Inference of Reionization Parameters from 3D Tomographic 21 cm Light-cone Images. *Astrophys. J.* **926**, 151 (2022). 2105.03344.
25. Zhao, X., Mao, Y. & Wandelt, B. D. Implicit Likelihood Inference of Reionization Parameters from the 21 cm Power Spectrum. *Astrophys. J.* **933**, 236 (2022). 2203.15734.
26. Zhao, X., Mao, Y., Zuo, S. & Wandelt, B. D. Simulation-based Inference of Reionization Parameters from 3D Tomographic 21 cm Light-cone Images – II: Application of Solid Harmonic Wavelet Scattering Transform (2023). 2310.17602.
27. Sun, T.-Y. *et al.* Efficient parameter inference for gravitational wave signals in the presence of transient noises using temporal and time-spectral fusion normalizing flow*. *Chin. Phys. C* **48**, 045108 (2024). 2312.08122.

28. Xiong, C.-Y., Sun, T.-Y., Zhang, J.-F. & Zhang, X. Robust inference of gravitational wave source parameters in the presence of noise transients using normalizing flows (2024). 2405.09475.
29. Nayak, P., Walther, M., Gruen, D. & Adiraju, S. Ly α NNA: A Deep Learning Field-level Inference Machine for the Lyman- α Forest (2023). 2311.02167.
30. Maitra, S., Cristiani, S., Viel, M., Trotta, R. & Cupani, G. Parameter estimation from Ly α forest in Fourier space using Information Maximising Neural Network (2024). 2404.04327.
31. Abdurashidova, Z. *et al.* Improved Constraints on the 21 cm EoR Power Spectrum and the X-Ray Heating of the IGM with HERA Phase I Observations. *Astrophys. J.* **945**, 124 (2023). 2210.04912.
32. Garzilli, A., Magalich, A., Ruchayskiy, O. & Boyarsky, A. How to constrain warm dark matter with the Lyman- α forest. *Mon. Not. Roy. Astron. Soc.* **502**, 2356–2363 (2021). 1912.09397.
33. Enzi, W. *et al.* Joint constraints on thermal relic dark matter from strong gravitational lensing, the Ly α forest, and Milky Way satellites. *Mon. Not. Roy. Astron. Soc.* **506**, 5848–5862 (2021). 2010.13802.
34. Villasenor, B., Robertson, B., Madau, P. & Schneider, E. New constraints on warm dark matter from the Lyman- α forest power spectrum. *Phys. Rev. D* **108**, 023502 (2023). 2209.14220.
35. Zelko, I. A. *et al.* Constraints on Sterile Neutrino Models from Strong Gravitational Lensing, Milky Way Satellites, and the Lyman- α Forest. *Phys. Rev. Lett.* **129**, 191301 (2022). 2205.09777.

36. Iršič, V. *et al.* Unveiling dark matter free streaming at the smallest scales with the high redshift Lyman-alpha forest. *Phys. Rev. D* **109**, 043511 (2024). 2309.04533.
37. Lin, J. Divergence measures based on the shannon entropy. *IEEE Transactions on Information Theory* **37**, 145–151 (1991).
38. Rao, C. R. Differential metrics in probability spaces. *Differential geometry in statistical inference* **10**, 217–240 (1987).
39. Lopes, R. H. C. *Kolmogorov-Smirnov Test*, 718–720 (Springer Berlin Heidelberg, Berlin, Heidelberg, 2011). URL https://doi.org/10.1007/978-3-642-04898-2_326.
40. More, A. Survey of resampling techniques for improving classification performance in unbalanced datasets. *arXiv preprint arXiv:1608.06048* (2016).
41. Banerjee, J. *et al.* Machine learning in rare disease. *Nature Methods* **20**, 803–814 (2023).
42. Mesinger, A., Furlanetto, S. & Cen, R. 21cmFAST: A Fast, Semi-Numerical Simulation of the High-Redshift 21-cm Signal. *Mon. Not. Roy. Astron. Soc.* **411**, 955 (2011). 1003.3878.
43. Yue, B. & Chen, X. Reionization in the warm dark matter model. *The Astrophysical Journal* **747**, 127 (2012).
44. Dayal, P., Choudhury, T. R., Bromm, V. & Pacucci, F. Reionization and galaxy formation in warm dark matter cosmologies. *The Astrophysical Journal* **836**, 16 (2017).
45. Cooray, A. & Sheth, R. K. Halo Models of Large Scale Structure. *Phys. Rept.* **372**, 1–129 (2002). astro-ph/0206508.

46. Zentner, A. R. The Excursion Set Theory of Halo Mass Functions, Halo Clustering, and Halo Growth. *Int. J. Mod. Phys. D* **16**, 763–816 (2007). [astro-ph/0611454](#).
47. Press, W. H. & Schechter, P. Formation of galaxies and clusters of galaxies by selfsimilar gravitational condensation. *Astrophys. J.* **187**, 425–438 (1974).
48. Smith, R. E. & Markovic, K. Testing the Warm Dark Matter paradigm with large-scale structures. *Phys. Rev. D* **84**, 063507 (2011). [1103.2134](#).
49. Shimabukuro, H., Ichiki, K. & Kadota, K. Constraining the nature of ultra light dark matter particles with the 21 cm forest. *Phys. Rev. D* **101**, 043516 (2020). [1910.06011](#).
50. Shimabukuro, H., Ichiki, K. & Kadota, K. Impact of dark matter-baryon relative velocity on the 21-cm forest. *Phys. Rev. D* **107**, 123520 (2023). [2212.08409](#).
51. Shimabukuro, H., Ichiki, K. & Kadota, K. 21 cm forest probes on axion dark matter in postinflationary Peccei-Quinn symmetry breaking scenarios. *Phys. Rev. D* **102**, 023522 (2020). [2005.05589](#).
52. Xu, Y., Yue, B. & Chen, X. Maximum Absorption of the Global 21 cm Spectrum in the Standard Cosmological Model. *Astrophys. J.* **923**, 98 (2021). [2102.12865](#).
53. Gnedin, N. Y. Effect of reionization on the structure formation in the universe. *Astrophys. J.* **542**, 535–541 (2000). [astro-ph/0002151](#).
54. Navarro, J. F., Frenk, C. S. & White, S. D. M. A Universal density profile from hierarchical clustering. *Astrophys. J.* **490**, 493–508 (1997). [astro-ph/9611107](#).

55. Barkana, R. A Model for infall around virialized halos. *Mon. Not. Roy. Astron. Soc.* **347**, 57 (2004). astro-ph/0212458.
56. Ripamonti, E., Mapelli, M. & Ferrara, A. The impact of dark matter decays and annihilations on the formation of the first structures. *Mon. Not. Roy. Astron. Soc.* **375**, 1399–1408 (2007). astro-ph/0606483.
57. Bhagwat, A., Ciardi, B., Zackrisson, E. & Schaye, J. Cospatial 21 cm and metal-line absorbers in the epoch of reionization – I. Incidence and observability. *Mon. Not. Roy. Astron. Soc.* **517**, 2331–2342 (2022). 2209.10573.
58. Madau, P., Meiksin, A. & Rees, M. J. 21-CM tomography of the intergalactic medium at high redshift. *Astrophys. J.* **475**, 429 (1997). astro-ph/9608010.
59. Field, G. B. An attempt to observe neutral hydrogen between the galaxies. *Astrophysical Journal*, vol. 129, p. 525 **129**, 525 (1959).
60. Aghanim, N. *et al.* Planck 2018 results. VI. Cosmological parameters. *Astron. Astrophys.* **641**, A6 (2020). [Erratum: *Astron. Astrophys.* 652, C4 (2021)], 1807.06209.
61. Thompson, A. R., Moran, J. M. & Swenson, G. W. *Interferometry and synthesis in radio astronomy* (Springer Nature, 2017).
62. Acedo, E. d. L., Pienaar, H. & Fagnoni, N. Antenna design for the SKA1-LOW and HERA super radio telescopes (2020). 2003.10733.

63. <https://www.skao.int/en/science-users/118/ska-telescope-specifications>.
64. Thyagarajan, N. Statistical Detection of IGM Structures during Cosmic Reionization using Absorption of the Redshifted 21 cm line by HI against Compact Background Radio Sources. *Astrophys. J.* **899**, 16 (2020). 2006.10070.
65. Papamakarios, G. & Murray, I. Fast ϵ -free inference of simulation models with bayesian conditional density estimation. *Advances in neural information processing systems* **29** (2016).
66. Csiszar, I. I -Divergence Geometry of Probability Distributions and Minimization Problems. *The Annals of Probability* **3**, 146 – 158 (1975). URL <https://doi.org/10.1214/aop/1176996454>.
67. Papamakarios, G., Sterratt, D. & Murray, I. Sequential neural likelihood: Fast likelihood-free inference with autoregressive flows. In *The 22nd International Conference on Artificial Intelligence and Statistics*, 837–848 (PMLR, 2019).
68. Durkan, C., Bekasov, A., Murray, I. & Papamakarios, G. Neural spline flows. *Advances in neural information processing systems* **32** (2019).
69. Glorot, X. & Bengio, Y. Understanding the difficulty of training deep feedforward neural networks. In *Proceedings of the thirteenth international conference on artificial intelligence and statistics*, 249–256 (JMLR Workshop and Conference Proceedings, 2010).
70. Loshchilov, I. & Hutter, F. Decoupled weight decay regularization. In *International Conference on Learning Representations* (2018).

71. Hoerl, A. E. & Kennard, R. W. Ridge regression: Biased estimation for nonorthogonal problems. *Technometrics* **12**, 55–67 (1970).
72. Fieller, E. C., Hartley, H. O. & Pearson, E. S. Tests for rank correlation coefficients. i. *Biometrika* **44**, 470–481 (1957).